Acta Astronautica 228 (2025) 494–514

Contents lists available at ScienceDirect

Acta Astronautica

journal homepage: www.elsevier.com/locate/actaastro

Research paper

Nonlinear adaptive angle-only relative navigation on perturbed eccentric orbits

Yazan Chihabi *, Steve Ulrich

Department of Mechanical and Aerospace Engineering, Carleton University, Ottawa, Ontario, Canada

ARTICLE INFO

Keywords:
Spacecraft formation flying
Guidance
Navigation
Control
Optimal guidance
Optimal control
Spacecraft experimentation

ABSTRACT

A novel angle-only relative navigation algorithm that utilizes both the extended and unscented Kalman filters for spacecraft relative motion is proposed in this paper. Specifically, the algorithms take advantage of a process model based on exact Hamiltonian dynamics that includes perturbations along with an exact measurement model that maps orbital elements to angle measurements. The proposed solution is tested in highly elliptical and low Earth orbits and compared against relative orbital elements based models, where the proposed model resulted in orders of magnitude increase in accuracy. Furthermore, due to the relationship between nonlinearities and increase in eccentricity of the orbit, the adaptive unscented Kalman filter demonstrated a larger increase in accuracy in the highly elliptical reference orbit case than the low Earth orbit.

1. Introduction

Ongoing worldwide space robotic activities and missions focus on the use of multiple spacecraft for formation flying, rendezvous and docking. This is a key technology for such missions as it offers lower costs and increased reliability by reducing the mass, power demand and size of the spacecraft buses. This reduction is a direct result of distributing functions and payloads among several small spacecraft. Among the many applications for spacecraft formation flying are the servicing and maintenance of existing satellites in orbit. Specifically, many proposals exist to refuel and repair damaged or otherwise considered obsolete satellites. In a historic, first of its kind mission with Northrop Grumman's spacecraft MEV-1,[1] Intelsat 901 (IS-901) communications satellite was returned to an operational state in late February, 2020. The main considerations are with respect to the guidance, navigation and control systems (GNandC), since they are responsible for calculating and controlling the desired relative motion between both vehicles.

Navigational instruments used in formation flying, such as GPS, are prone to noise, drift, and other adverse effects. To solve this problem, several filtering techniques have been proposed. Amongst them, Kalman-based filtering represents the most popular navigational solution employed with formation flying missions. The Kalman filter is a method to design optimal state observers or estimators by taking advantage of probability distributions. In other words, it can either find the best estimate of a value that cannot be measured directly or provides an optimal measurement of states by combining different sensor measurements which are subject to noise and inaccuracies. The efficiency of Kalman-based relative navigation filters have been demonstrated in various missions such as PRISMA [1], CanX-4/5 [2,3], and AVANTI [4], which were able to maintain control accuracies at the sub-meter level and thereby present a new host of possibilities for the safe utilization of co-orbiting, cooperative formations.

More recently, Fraser and Ulrich [5] proposed methodologies for adaptive extended Kalman filtering, which are suitable for spacecraft formation flying on non-Keplerian low Earth orbits. The adaptive extended Kalman filter (EKF) algorithm used Maximum Likelihood Estimation (MLE) to develop adaptation mechanisms for the process and measurement noise covariance matrices used within the filter. The objective of the MLE routine was to maximize the likelihood that the observed measurements corresponded to the current tuning of the EKF, and the adaptation laws were derived through the residuals covariance matrix of the filter. Furthermore, intrinsic smoothing was incorporated into the MLE algorithm for improving the accuracy of covariance matrix prediction. The adaptive EKF methods proposed by the authors [5] were shown to produce relative position and velocity estimates that were more accurate than estimates provided by a standard, non-adaptive EKF.

However, the relative navigation algorithm employed by Fraser and Ulrich [5] relies on GPS measurements of both the target and chaser spacecraft, which can pose an issue in non-cooperative scenarios

* Corresponding author.
E-mail address: Yazanchihabi@cmail.carleton.ca (Y. Chihabi).

[1] https://news.northropgrumman.com/news/releases.

https://doi.org/10.1016/j.actaastro.2024.12.012
Received 7 February 2024; Accepted 7 December 2024
Available online 17 December 2024

where target GPS measurements are unavailable. In such scenarios, a common solution utilizes monocular cameras to determine relative states based on angle-only measurements. The use of angles-only navigation for orbital rendezvous and docking, spacecraft formation flight, and other relative motion applications have been demonstrated by several space missions with increasingly demanding relative navigation requirements that must be achieved autonomously using limited onboard resources [6]. Angle-only relative navigation using a single camera (monocular vision) sensor provides an inherently passive, robust, and high-dynamic range capability due to their low-cost, low power consumption, and small size as compared with other systems such as LIDAR and RADAR [4,7]. According to these contributions, applying maneuvers along the line-of-sight vector renders the system observable. Indeed, the angles-only navigation problem is not fully observable in the absence of maneuvers [6,8,9]. Of particular interest in this research is an active chaser attempting rendezvous from large separation distances (on the order of hundreds of kilometers) with a non-cooperative target spacecraft relying primarily on an angle-only relative navigation solution.

Most relative navigation algorithms rely on Keplerian nonlinear equations of motion in the cartesian frame within an EKF. Such formulations result in errors due to neglecting perturbations within the dynamical model and linearizations of the process and measurement models of the estimation algorithm [7]. To overcome the linearization of the measurement model, Sullivan and D'amico [10] employed the unscented Kalman filter (UKF) to enhance dynamical observability and filter performance. The authors utilized a relative orbital elements (ROE) based linear dynamical model to further improve observability during maneuvers. Indeed, the unobservability of the relative navigation problem is only in one component of the states: the relative argument of latitude [7]. The ROE model used by the authors takes into account secular (mean) variations due to J_2, solar radiation pressure, atmospheric drag, and luni-solar third-body perturbations [11]. Furthermore, Sullivan et al. [11] further developed the algorithm into a generalized architecture for relative navigation with multiple targets which was tested on in partnership with NASA on the Starling Formation-flying Optical eXperiment; a hardware-in-the-loop experimental testbed. For all cases, the algorithms proposed by the authors were tested for passive formation flying scenarios using first-order Gauss' Variational Equations to propagate perturbing effects. However, the ROE dynamical model is limited by the small-angle assumption which would result in reduced accuracy for large relative orbital elements. Furthermore, their proposed model does not considers periodic variations of orbital elements for all perturbations, and only takes into account mean-to-osculating conversion due to J_2, further reducing the accuracy of the estimation schemes. In addition, first-order approximated equations relating ROEs to cartesian coordinates developed by Schaub et al. [12, p. 593–673] were used to formulate the measurement models for all aforementioned angle-only relative navigation algorithms. The authors incorporated an adaptive algorithm for covariance tuning using the innovation covariance matching technique [13] which is similar to Fraser and Ulrich's MLE algorithm but without the intrinsic smoothing.

In this context, the main contributions of this paper are: (1) development of extended and unscented Kalman filtering algorithms using nonlinear Hamiltonian dynamics that captures the full periodic effects of J_2, luni-solar third-body, solar radiation pressure and atmospheric drag perturbations [14] (2) the utilization of exact nonlinear dynamics in the measurement model that relates orbital elements to angle-only measurements and (3) extension of the maximum likelihood estimation adaptive algorithm with intrinsic smoothing developed by [5] to angle-only relative navigation. The nonlinear dynamics utilized in the development of the measurement model is based on Gurfil and Kholshevnikov's equations of motion [15,16]. In addition, the algorithms proposed in this work are validated in simulation using exact Cartesian nonlinear equations of motion under the effects of perturbations, unlike in [7,10] which was validated using first-order Gauss' Variational Equations.

This paper is organized as follows: Section 2 describes the mathematical preliminaries pertaining to the unscented and extended Kalman filtering algorithms as well as the reference frames used in the development of the measurement model. Next, Section 3 describes the derivation and development of the relative navigation algorithms. Section 4 presents results for far-range relative navigation scenarios in both low Earth orbit (LEO) and highly elliptical orbit (HEO) and concluding remarks are provided in Section 5.

2. Preliminaries

For completeness, this section provides the mathematical preliminaries for the EKF and UKF techniques, along with adaptive covariance tuning. In addition, the relevant reference frames are defined within this section.

2.1. Kalman filtering

Most systems, if not all, are characterized by a system of non-linear equations. As a result, applying a linear Kalman filter is not sufficient to provide accurate estimations of states. A non-linear system is defined by

$$\dot{\boldsymbol{x}}(t) = \boldsymbol{f}(\boldsymbol{x}, \boldsymbol{u}, t) + \boldsymbol{w}(t) \tag{1}$$

$$\boldsymbol{y}(t) = \boldsymbol{h}(\boldsymbol{x}, t) + \boldsymbol{v}(t) \tag{2}$$

where $\boldsymbol{x}$ are the states, $\boldsymbol{y}$ is the measurement output and $\boldsymbol{w}$ and $\boldsymbol{v}$ are the process and measurement noise respectively. Function $\boldsymbol{f}$ is a nonlinear function that relates the states at the previous time step $k-1$ to the states at the current time-step k whereas function $\boldsymbol{h}$ relates the current states to the current measurements. The extended Kalman filter equations are given by [17]

$$\hat{\boldsymbol{x}}_k^- = \hat{\boldsymbol{x}}_{k-1} + \int_{t_{k-1}}^{t_k} \boldsymbol{f}(\hat{\boldsymbol{x}}_{k-1}, \boldsymbol{u}_{k-1}, t)dt \tag{3}$$

$$\boldsymbol{P}_k^- = \boldsymbol{\Phi}_k \boldsymbol{P}_{k-1}^+ \boldsymbol{\Phi}_k^T + \boldsymbol{Q}_{k-1} \tag{4}$$

$$\boldsymbol{K}_k = \boldsymbol{P}_k^- \boldsymbol{H}_k^T (\boldsymbol{H}_k \boldsymbol{P}_k^- \boldsymbol{H}_k^T + \boldsymbol{R}_{k-1})^{-1} \tag{5}$$

$$\hat{\boldsymbol{x}}_k^+ = \hat{\boldsymbol{x}}_k^- + \boldsymbol{K}_k(\boldsymbol{y}_k - \boldsymbol{h}(\hat{\boldsymbol{x}}_k^-, \boldsymbol{0})) \tag{6}$$

$$\boldsymbol{P}_k^+ = (\boldsymbol{I} - \boldsymbol{K}_k \boldsymbol{H}_k)\boldsymbol{P}_k^-(\boldsymbol{I} - \boldsymbol{K}_k \boldsymbol{H}_k)^T + \boldsymbol{K}_k \boldsymbol{R}_k \boldsymbol{K}_k^T \tag{7}$$

where $\boldsymbol{H}$ is given by

$$\boldsymbol{H} = \frac{\partial \boldsymbol{h}}{\partial \boldsymbol{x}}(\hat{\boldsymbol{x}}_k, 0) \tag{8}$$

and where state transition matrix, $\boldsymbol{\Phi}_k$, is calculated as follows

$$\boldsymbol{\Phi} = \boldsymbol{I} + \boldsymbol{F}_{k-1}\Delta t + \frac{\boldsymbol{F}_{k-1}^2 \Delta t^2}{2!} + \frac{\boldsymbol{F}_{k-1}^3 \Delta t^3}{3!} + .., \tag{9}$$

$$\boldsymbol{F}_{k-1} = \frac{\partial \boldsymbol{f}}{\partial \boldsymbol{x}}(\hat{\boldsymbol{x}}_{k-1}, \boldsymbol{u}_{k-1}) \tag{10}$$

with $\Delta t = t_k - t_{k-1}$.

2.2. Unscented Kalman filter

The EKF algorithm provides a first order approximation to the optimal state estimation problem by linearizing the nonlinear process and measurement models [18]. An alternative approach, known as the unscented Kalman filter, avoids this issue by propagating Gaussian random variables (GRV) using sample points known as sigma points [18,19]. These sigma points are found using the prior estimates according to the following equations

$$\mathcal{X}_0 = \bar{\boldsymbol{x}} \tag{11}$$

$$\mathcal{X}_i = \bar{\boldsymbol{x}} + \left(\sqrt{(L+\lambda)\boldsymbol{P}}\right)_i \quad i = 1, \ldots, L \tag{12}$$

$$\mathcal{X}_i = \bar{\boldsymbol{x}} - \left(\sqrt{(L+\lambda)\boldsymbol{P}}\right)_i \quad i = L+1, \ldots, 2L \tag{13}$$

where L is the dimension of the state vector $\boldsymbol{x}$ and the square root of the matrix $\boldsymbol{P}$ is found by taking the ith column of lower triangular Cholesky factorization of the matrix. A matrix $\boldsymbol{\mathcal{X}}$ of sigma vectors can be formed as

$$\boldsymbol{\mathcal{X}}_{k-1} = \begin{bmatrix} \hat{\boldsymbol{x}}_{k-1} & \hat{\boldsymbol{x}}_{k-1} + \gamma\sqrt{\boldsymbol{P}_{k-1}} & \hat{\boldsymbol{x}}_{k-1} - \gamma\sqrt{\boldsymbol{P}_{k-1}} \end{bmatrix} \tag{14}$$

where $\gamma = \sqrt{L+\lambda}$ and λ is the composite scaling parameter determined by $\lambda = \alpha^2(L+\kappa) - L$. The variable α determines the spread of the sigma points around the mean states and is usually set to a small positive value (e.g., 1e-3) and κ is a secondary scaling parameter which is usually set to 0. The time update equations are given by

$$\boldsymbol{\mathcal{X}}_{k|k-1} = \boldsymbol{\mathcal{X}}_{k-1} + \int_{t_{k-1}}^{t_k} \boldsymbol{f}(\boldsymbol{\mathcal{X}}_{k-1}, \boldsymbol{u}_{k-1}, t)dt \tag{15}$$

$$\hat{\boldsymbol{x}}_k^- = \sum_{i=0}^{2L} W_i^{(m)} \mathcal{X}_{i,k|k-1} \tag{16}$$

$$\boldsymbol{P}_k^- = \sum_{i=0}^{2L} W_i^{(c)} \left[\mathcal{X}_{i,k|k-1} - \hat{\boldsymbol{x}}_k^-\right]\left[\mathcal{X}_{i,k|k-1} - \hat{\boldsymbol{x}}_k^-\right]^T + \boldsymbol{Q} \tag{17}$$

$$\boldsymbol{\mathcal{Y}}_{k|k-1} = \boldsymbol{h}(\boldsymbol{\mathcal{X}}_{k|k-1}) \tag{18}$$

$$\hat{\boldsymbol{y}}_k^- = \sum_{i=0}^{2L} W_i^{(m)} \mathcal{Y}_{i,k|k-1} \tag{19}$$

where

$$W_0^{(m)} = \lambda/(L+\lambda) \tag{20}$$

$$W_0^{(n)} = \lambda/(L+\lambda) + (1 - \alpha^2 + \beta) \tag{21}$$

$$W_i^{(m)} = W_i^{(n)} = 1/\{2(L+\lambda)\} \quad i = 1, \ldots, 2L \tag{22}$$

and β is used to incorporate prior knowledge of the distribution of $\boldsymbol{x}$ (for Gaussian distributions, $\beta = 2$ is optimal). The measurement update equations are then given by

$$\boldsymbol{P}_{\boldsymbol{y}_k\boldsymbol{y}_k} = \sum_{i=0}^{2L} W_i^{(c)} \left[\mathcal{Y}_{i,k|k-1} - \hat{\boldsymbol{y}}_k^-\right]\left[\mathcal{Y}_{i,k|k-1} - \hat{\boldsymbol{y}}_k^-\right]^T + \boldsymbol{R} \tag{23}$$

$$\boldsymbol{P}_{\boldsymbol{x}_k\boldsymbol{y}_k} = \sum_{i=0}^{2L} W_i^{(c)} \left[\mathcal{X}_{i,k|k-1} - \hat{\boldsymbol{x}}_k^-\right]\left[\mathcal{Y}_{i,k|k-1} - \hat{\boldsymbol{y}}_k^-\right]^T \tag{24}$$

$$\boldsymbol{K}_k = \boldsymbol{P}_{\boldsymbol{x}_k\boldsymbol{y}_k}\boldsymbol{P}_{\boldsymbol{y}_k\boldsymbol{y}_k}^{-1} \tag{25}$$

$$\hat{\boldsymbol{x}}_k^+ = \hat{\boldsymbol{x}}_k^- + \boldsymbol{K}_k(\boldsymbol{y}_k - \hat{\boldsymbol{y}}_k^-) \tag{26}$$

$$\boldsymbol{P}_k^+ = \boldsymbol{P}_k^- - \boldsymbol{K}_k\boldsymbol{P}_{\boldsymbol{y}_k\boldsymbol{y}_k}\boldsymbol{K}_k^T \tag{27}$$

2.3. Covariance adaptation using maximum likelihood estimation

Kalman filters is essentially a recursive algorithm that depends only on estimates from the previous time step. As such, the incorporation of a set of previous estimates and measurements may provide further improvement to the accuracy of the algorithms [5,20]. Fraser and Ulrich [5] provide an adaptation method for process and measurement covariance tuning based on maximum likelihood estimation (MLE) with intrinsic smoothing that provides optimal values of the matrices by running backward through a window of size N, which contains the set of data points from $i_0 = k - N + 1$ to the latest point k. Initial smoothed estimates are taken from the filter at the current time step as $\hat{\boldsymbol{x}}_{N|N} = \hat{\boldsymbol{x}}_k^+$ and $\boldsymbol{P}_{N|N} = \hat{\boldsymbol{P}}_k^+$, where the smoothed state estimate at time t_k given N past data points is denoted by $\hat{\boldsymbol{x}}_{k|N}$. Using these initial conditions, the smoothed state and error covariances within the memory window for data from $k = N-1, N-2, \ldots, i_0$ are calculated using

$$\boldsymbol{G}_{k-1} = \boldsymbol{P}_{k-1}^+\boldsymbol{\Phi}_k^T\left(\boldsymbol{P}_k^-\right)^{-1} \tag{28}$$

$$\hat{\boldsymbol{x}}_{k-1|N} = \hat{\boldsymbol{x}}_{k-1}^+ + \boldsymbol{G}_{k-1}\left(\hat{\boldsymbol{x}}_{k|N} - \hat{\boldsymbol{x}}_k^-\right) \tag{29}$$

$$\boldsymbol{P}_{k-1|N} = \boldsymbol{P}_{k-1}^+ + \boldsymbol{G}_{k-1}\left(\boldsymbol{P}_{k|N} - \boldsymbol{P}_k^-\right)\boldsymbol{G}_{k-1}^T \tag{30}$$

where $\boldsymbol{G}_k \in \mathbb{R}^{n\times m}$ is a smoothing gain derived as the MLE estimator for the current state estimates given the entire set of measurements available [21]. The adaptation equations for the process and measurement covariance matrices is then given as

$$\hat{\boldsymbol{Q}}_k = \boldsymbol{K}_k\left[\frac{1}{N}\sum_{i=i_0}^{N}\left(\boldsymbol{z}_i - \hat{\boldsymbol{z}}_{i|N}\right)\left(\boldsymbol{z}_i - \hat{\boldsymbol{z}}_{i|N}\right)^T\right]\boldsymbol{K}_k^T \tag{31}$$

$$\hat{\boldsymbol{R}}_k = \frac{1}{N}\sum_{i=i_0}^{N}\left[\left(\boldsymbol{z}_i - \hat{\boldsymbol{z}}_{i|N}\right)\left(\boldsymbol{z}_i - \hat{\boldsymbol{z}}_{i|N}\right)^T + \boldsymbol{H}_{i|N}\boldsymbol{P}_{i|N}^+\boldsymbol{H}_{i|N}^T\right] \tag{32}$$

where

$$\hat{\boldsymbol{z}}_{i|N} = \boldsymbol{h}(\hat{\boldsymbol{x}}_{k|N}) \tag{33}$$

and $\boldsymbol{H}_{i|N}$ is evaluated using smoothed state estimates.

2.4. Reference frames

In this work, three references frames are required to derive equations of relative motion: the Earth-centered inertial (ECI), the perifocal and finally the local-vertical-local-horizon (LVLH) reference frames.

The ECI reference frame is denoted by $\mathcal{F}_I$ and defined by its orthonormal unit vectors $[\vec{I}_x, \vec{I}_y, \vec{I}_z]^T$ with its origin at the center of Earth. The unit vector $\vec{I}_z$ is aligned with the Earth's axis of rotation in the direction of the North Pole, and $\vec{I}_x$ and $\vec{I}_y$ lie on the Earth's equatorial plane. Furthermore, $\vec{I}_x$ points in the direction of the vernal equinox with $\vec{I}_y$ completing the triad such that the reference frame remains fixed in space and $\vec{I}_y = \vec{I}_z \times \vec{I}_x$.

The perifocal reference frame is denoted by $\mathcal{F}_p$ and defined by its orthonormal unit vectors $[\vec{P}_x, \vec{P}_y, \vec{P}_z]^T$ with its origin also at the center of Earth. The unit vector $\vec{P}_z$ points in the same direction as the orbit's angular momentum vector normal to the orbital plane, $\vec{P}_x$ and $\vec{P}_y$ lie on the orbital plane with $\vec{P}_x$ pointing in the direction of the perigee, and $\vec{P}_y$ completing the triad such that $\vec{P}_y = \vec{P}_z \times \vec{P}_x$. For the purposes of this paper, two perifocal reference frames are used and denoted as $\mathcal{F}_p^t$ and $\mathcal{F}_p^c$ for the target and chaser orbit respectively.

Finally, the LVLH reference frame is denoted by $\mathcal{F}_L$ and defined by its orthonormal unit vectors $[\vec{L}_x, \vec{L}_y, \vec{L}_z]^T$ with its origin at the target spacecraft. The unit vector $\vec{L}_z$ points in the same direction as the orbit's angular momentum vector normal to the orbital plane. $\vec{L}_x$ points in the direction of the target's inertial position $\vec{r}_t$ and $\vec{L}_y$ completing the triad such that $\vec{L}_y = \vec{L}_z \times \vec{L}_x$. Similarly, the chaser's LVLH reference frame denoted by $\mathcal{F}_{L_c}$ can be expressed by instead defining the origin at the chaser spacecraft.

3. Relative navigation formulation

This section presents the derivation of the relative navigation process and measurement models.

3.1. Process model

The nonlinear dynamics of spacecraft orbital motion can be expressed in terms of orbital elements as

$$\dot{\boldsymbol{oe}} = \begin{bmatrix} \dot{a} & \dot{e} & \dot{i} & \dot{\omega} & \dot{\Omega} & \dot{M} \end{bmatrix}^T = \boldsymbol{f}(\boldsymbol{oe}) \tag{34}$$

where a, e, Ω, i, ω, and M are the semi-major axis, eccentricity, right ascension of the ascending node (RAAN), inclination, and argument of perigee, and mean anomaly of the spacecraft, respectively. The unforced dynamics, $\boldsymbol{f}(\boldsymbol{oe})$, is a combination of Keplerian and total perturbing effects considered represented by

$$\boldsymbol{f}(\boldsymbol{oe}) = \boldsymbol{f}_{kep}(\boldsymbol{oe}) + \sum \boldsymbol{f}_p(\boldsymbol{oe}) \tag{35}$$

where

$$\boldsymbol{f}_{kep}(\boldsymbol{oe}) = \begin{bmatrix} 0 & 0 & 0 & 0 & 0 & n \end{bmatrix}^T \tag{36}$$

$$\boldsymbol{f}_p(\boldsymbol{oe}) = \begin{bmatrix} \dot{a}_p & \dot{e}_p & \dot{i}_p & \dot{\omega}_p & \dot{\Omega}_p & \dot{M}_p \end{bmatrix}^T \tag{37}$$

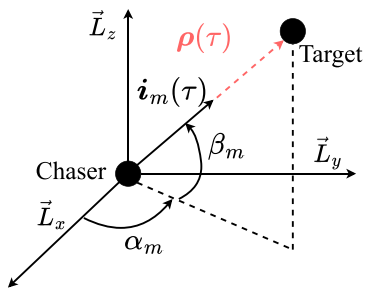

Fig. 1. LOS angle measurements.

where subscript p denotes the perturbed orbital elements. The orbital motion of the chaser and the target spacecraft can be grouped together to form the process dynamics using the previous equations as

$$\dot{\boldsymbol{x}} = \boldsymbol{f}(\boldsymbol{\alpha e}_t) \tag{38}$$

such that $\boldsymbol{x} = \boldsymbol{\alpha e}_t$. The process model Jacobian of the previous equation is therefore expressed as

$$\boldsymbol{F}(t) = \left.\frac{\partial \boldsymbol{f}(\boldsymbol{\alpha e})}{\partial \boldsymbol{\alpha e}}\right|_{\boldsymbol{\alpha e}=\boldsymbol{\alpha e}_t} \tag{39}$$

The matrices that make up the Jacobian matrix, $\boldsymbol{F}(t)$, are given in Chihabi and Ulrich [14,22] and contain the perturbing effects of J_2, Luni-solar third-body, solar radiation pressure, and atmospheric drag.

3.2. Measurement model

The angle-only measurements are taken with respect to the chaser spacecraft, therefore, the relative position vector of the target spacecraft with respect to the chaser, denoted as $\vec{\rho}$, is defined as

$$\vec{\rho} = \vec{r}_t - \vec{r}_c \tag{40}$$

where $\vec{r}_c$ and $\vec{r}_t$ respectively denote the position vectors of the chaser and target spacecraft. Expressed as components in the chaser's LVLH reference frame, Eq. (40) becomes

$$\boldsymbol{\rho}_{L_c} = \boldsymbol{r}_{t_{L_c}} - \boldsymbol{r}_{c_{L_c}} \tag{41}$$

where $\boldsymbol{r}_{c_{L_c}}$ and $\boldsymbol{r}_{t_{L_c}}$ are the position vector components of the chaser and target spacecraft expressed in $\mathcal{F}_{L_c}$. The angle measurements can be written as a LOS unit vector measurement $\boldsymbol{i}_m$ equivalent to the unit vector of the position of the target with respect to the chaser based on the description in Fig. 1, that is [6],

$$\boldsymbol{i}_m = \frac{\boldsymbol{\rho}_{L_c}}{\|\boldsymbol{\rho}_{L_c}\|} = \begin{bmatrix} \cos(\alpha_m)\cos(\beta_m) \\ \sin(\alpha_m)\cos(\beta_m) \\ \sin(\beta_m) \end{bmatrix} \tag{42}$$

such that

$$\alpha_m = \alpha + \upsilon_\alpha \tag{43}$$

$$\beta_m = \beta + \upsilon_\beta \tag{44}$$

wbere υ_α and υ_β denote the sensor noise contribution to the angle measurements.

To find the position vector components of the target spacecraft in the chaser's LVLH reference frame, two rotation matrices are required. The first rotation matrix converts the position vector components in $\mathcal{F}_p^t$ to $\mathcal{F}_I$ using $\boldsymbol{C}_{IP_t}(\omega_t, i_t, \Omega_t)$ defined as a 3-1-3 rotation sequence given by

$$\boldsymbol{C}_{IP_t}(\omega_t, i_t, \Omega_t) = \begin{bmatrix} c_{\Omega_t}c_{\omega_t} - s_{\Omega_t}s_{\omega_t}c_{i_t} & -c_{\Omega_t}s_{\omega_t} - s_{\Omega_t}c_{\omega_t}c_{i_t} & s_{\Omega_t}s_{i_t} \\ s_{\Omega_t}c_{\omega_t} + c_{\Omega_t}s_{\omega_t}c_{i_t} & -s_{\Omega_t}s_{\omega_t} - c_{\Omega_t}c_{\omega_c}c_{i_t} & -c_{\Omega_t}s_{i_t} \\ s_{\omega_t}s_{i_t} & c_{\omega_t}s_{i_t} & c_{i_t} \end{bmatrix} \tag{45}$$

The second rotation matrix, $\boldsymbol{C}_{LI}$, converts the position vector components of the target spacecraft in $\mathcal{F}_I$ to $\mathcal{F}_P^c$ using $\boldsymbol{C}_{P_cI}(\omega_c, i_c, \Omega_c)$ given by

$$\boldsymbol{C}_{P_cI}(\omega_c, i_c, \Omega_c) = \begin{bmatrix} c_{\Omega_c}c_{\omega_c} - s_{\Omega_c}s_{\omega_c}c_{i_c} & s_{\Omega_c}c_{\omega_c} + c_{\Omega_c}s_{\omega_c}c_{i_c} & s_{\omega_c}s_{i_c} \\ -c_{\Omega_c}s_{\omega_c} - s_{\Omega_c}c_{\omega_c}c_{i_c} & -s_{\Omega_c}s_{\omega_c} - c_{\Omega_c}c_{\omega_c}c_{i_c} & c_{\omega_c}s_{i_c} \\ s_{\Omega_c}s_{i_c} & -c_{\Omega_c}s_{i_c} & c_{i_c} \end{bmatrix} \tag{46}$$

such that $\boldsymbol{C}_{IP}(\omega, i, \Omega) = \boldsymbol{C}_{PI}^T(\omega, i, \Omega)$, and from $\mathcal{F}_P^c$ to $\mathcal{F}_L^c$ using $\boldsymbol{C}_{L_cP_c}(\theta_c)$ given by

$$\boldsymbol{C}_{L_cP_c}(\theta_c) = \begin{bmatrix} c_{\theta_c} & s_{\theta_c} & 0 \\ -s_{\theta_c} & c_{\theta_c} & 0 \\ 0 & 0 & 1 \end{bmatrix} \tag{47}$$

where θ_c denotes the true anomaly of the chaser such that

$$\boldsymbol{r}_{t_{L_c}} = \boldsymbol{C}_{L_cP_c}(\theta_c)\boldsymbol{C}_{P_cI}(\omega_c, i_c, \Omega_c)\boldsymbol{C}_{IP_t}(\omega_t, i_t, \Omega_t)\boldsymbol{r}_{t_{P_t}} \tag{48}$$

$$\boldsymbol{r}_{c_{L_c}} = \begin{bmatrix} r_c & 0 & 0 \end{bmatrix}^T \tag{49}$$

where $\boldsymbol{r}_{t_{P_t}}$ denotes the position vector components of the chaser spacecraft in $\mathcal{F}_p^t$ given by

$$\boldsymbol{r}_{t_P} = \begin{bmatrix} r_t\cos\theta_t & r_t\sin\theta_t & 0 \end{bmatrix}^T \tag{50}$$

and r_t and r_c are calculated using the orbit equation

$$r = \frac{a(1-e^2)}{1 + e\cos\theta} \tag{51}$$

Since the equations shown above are functions of the true anomaly, θ, a way of computing it is required. A simple recursive solution is given by

$$E = M + e\sin(M + e\sin(M + e\sin(M + \cdots + e\sin(M)))) \tag{52}$$

$$\cos\theta = \frac{\cos E - e}{1 - e\cos E} \tag{53}$$

$$\sin\theta = \frac{\sqrt{1-e^2}\sin E}{1 - e\cos E} \tag{54}$$

$$\theta = \tan^{-1}\frac{\sin\theta}{\cos\theta} \tag{55}$$

where E is the eccentric anomaly and M is the mean anomaly. This is a recursive solution based on the Newton–Raphson Iteration Technique[2] which implies an infinite series. Therefore, a term will be truncated based on the desired accuracy. Now, the measurement model can herein be defined as the line of sight unit vector from the chaser to the target spacecraft as

$$\boldsymbol{y}(t) = \boldsymbol{i}_m = \frac{\boldsymbol{\rho}_{L_c}}{\|\boldsymbol{\rho}_{L_c}\|} = \frac{\boldsymbol{r}_{t_{L_c}} - \boldsymbol{r}_{c_{L_c}}}{\|\boldsymbol{r}_{t_{L_c}} - \boldsymbol{r}_{c_{L_c}}\|} = \boldsymbol{h}(\boldsymbol{x}) \tag{56}$$

Taking into consideration that $\boldsymbol{r}_{c_{L_c}}$ is only a function of a_c, e_c and θ_c, the Jacobian of the measurement dynamics is herein derived as

$$\begin{aligned} \boldsymbol{H}(\boldsymbol{x}) &= \frac{\partial}{\partial \boldsymbol{x}}\frac{\boldsymbol{r}_{t_{L_c}} - \boldsymbol{r}_{c_{L_c}}}{\|\boldsymbol{r}_{t_{L_c}} - \boldsymbol{r}_{c_{L_c}}\|} \\ &= \frac{1}{\|\boldsymbol{r}_{t_{L_c}} - \boldsymbol{r}_{c_{L_c}}\|}\left(\frac{\partial}{\partial \boldsymbol{\alpha e}_t}\boldsymbol{r}_{t_{L_c}}\right) + \left(\boldsymbol{r}_{t_{L_c}} - \boldsymbol{r}_{c_{L_c}}\right)\left(\frac{\partial}{\partial \boldsymbol{\alpha e}_t}\frac{1}{\|\boldsymbol{r}_{t_{L_c}} - \boldsymbol{r}_{c_{L_c}}\|}\right) \end{aligned} \tag{57}$$

The partial derivatives contained within the previous equation can be written as

$$\frac{\partial}{\partial \boldsymbol{\alpha e}_t}\boldsymbol{r}_{t_{L_c}} = \begin{bmatrix} H^1_{1,1} & H^1_{1,2} & H^1_{1,3} & H^1_{1,4} & H^1_{1,5} & H^1_{1,6} \\ H^1_{2,1} & H^1_{2,2} & H^1_{2,3} & H^1_{2,4} & H^1_{2,5} & H^1_{2,6} \\ H^1_{3,1} & H^1_{3,2} & H^1_{3,3} & H^1_{3,4} & H^1_{3,5} & H^1_{3,6} \end{bmatrix} \tag{58}$$

[2] http://web.mit.edu/10.001/Web/Course_Notes/NLAE/node6.html.

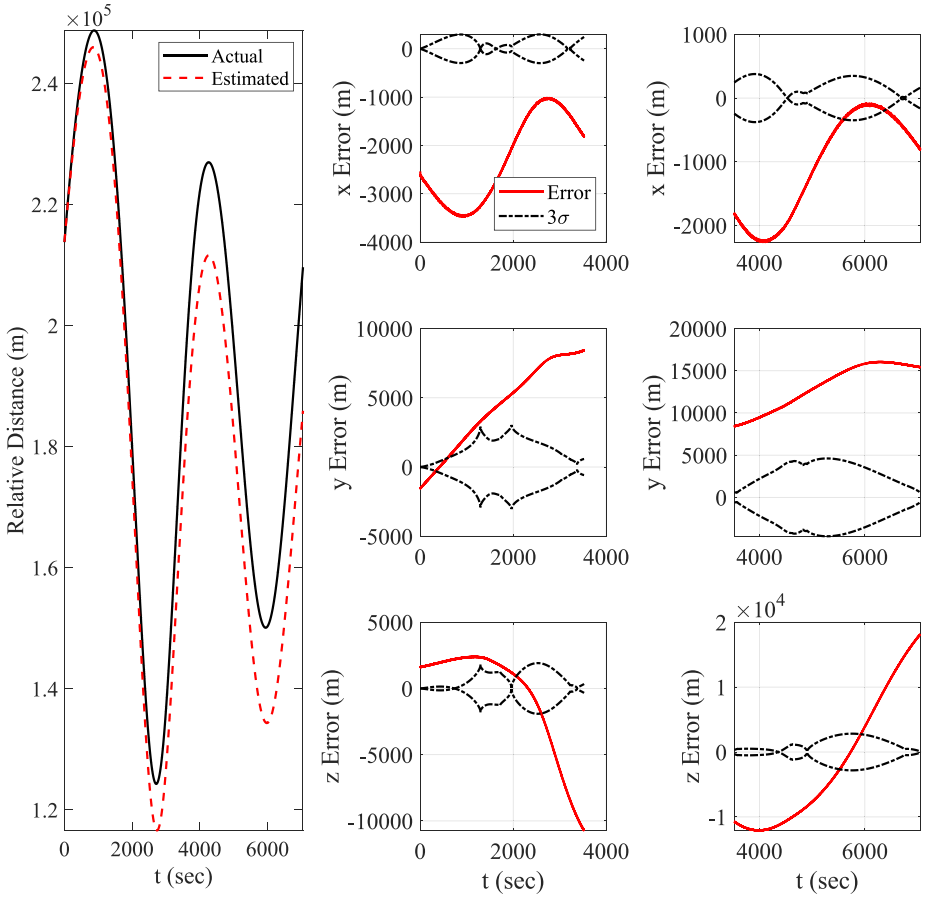

Fig. 2. LEO EKF estimation errors using ROE dynamics and measurement model.

$$\frac{\partial}{\partial \boldsymbol{\alpha}_t}\frac{1}{\|\boldsymbol{r}_{t_{L_c}}-\boldsymbol{r}_{c_{L_c}}\|}=\begin{bmatrix}\frac{H^2_{nu,1}}{H^2_{de,1}} & \frac{H^2_{nu,2}}{H^2_{de,2}} & \frac{H^2_{nu,3}}{H^2_{de,3}} & \frac{H^2_{nu,4}}{H^2_{de,4}} & \frac{H^2_{nu,5}}{H^2_{de,5}} & \left(\frac{\partial\theta}{\partial M}\right)_t & \frac{H^2_{nu,6}}{H^2_{de,6}}\end{bmatrix} \tag{59}$$

where

$$\begin{bmatrix}H^1_{1,1}\\H^1_{2,1}\\H^1_{3,1}\end{bmatrix}=\left(\frac{\partial r}{\partial a}\right)_t \boldsymbol{C}_{L_cP_c}(\theta_c)\boldsymbol{C}_{P_cI}(\omega_c,i_c,\Omega_c)\boldsymbol{C}_{IP_t}(\omega_t,i_t,\Omega_t)\begin{bmatrix}\cos\theta_t\\\sin\theta_t\\0\end{bmatrix} \tag{60}$$

$$\begin{bmatrix}H^1_{1,2}\\H^1_{2,2}\\H^1_{3,2}\end{bmatrix}=\left(\frac{\partial r}{\partial e}\right)_t \boldsymbol{C}_{L_cP_c}(\theta_c)\boldsymbol{C}_{P_cI}(\omega_c,i_c,\Omega_c)\boldsymbol{C}_{IP_t}(\omega_t,i_t,\Omega_t)\begin{bmatrix}\cos\theta_t\\\sin\theta_t\\0\end{bmatrix} \tag{61}$$

$$\begin{bmatrix}H^1_{1,i}\\H^1_{2,i}\\H^1_{3,i}\end{bmatrix}=\boldsymbol{C}_{L_cP_c}(\theta_c)\boldsymbol{C}_{P_cI}(\omega_c,i_c,\Omega_c)\left[\frac{\partial}{\partial(\cdot)}\boldsymbol{C}_{IP_t}(\omega_t,i_t,\Omega_t)\right]\boldsymbol{r}_{t_{P_t}} \tag{62}$$

$$\begin{aligned}\begin{bmatrix}H^1_{16}\\H^1_{26}\\H^1_{36}\end{bmatrix}&=\left(\frac{\partial\theta}{\partial M}\right)_t\left(\frac{\partial r}{\partial\theta}\right)_t \boldsymbol{C}_{L_cP_c}(\theta_c)\boldsymbol{C}_{P_cI}(\omega_c,i_c,\Omega_c)\boldsymbol{C}_{IP_t}(\omega_t,i_t,\Omega_t)\begin{bmatrix}\cos\theta_t\\\sin\theta_t\\0\end{bmatrix}\\&+r_t\left(\frac{\partial\theta}{\partial M}\right)_t \boldsymbol{C}_{L_cP_c}(\theta_c)\boldsymbol{C}_{P_cI}(\omega_c,i_c,\Omega_c)\boldsymbol{C}_{IP_t}(\omega_t,i_t,\Omega_t)\begin{bmatrix}-\sin\theta_t\\\cos\theta_t\\0\end{bmatrix}\end{aligned} \tag{63}$$

and the partial derivatives contained within the previous equations are provided in Appendix A. Furthermore, Eq. (59) is derived using MATLAB symbolic and are given in the Appendix B.

4. Results

This section presents a comparison of proposed adaptive Kalman filter algorithm developed in the previous section against a numerical propagator that integrates the exact nonlinear differential equations of motion in the inertial reference frame to verify the accuracy of the model. Specifically, the adaptive Kalman filtering algorithm is compared against a benchmark extended Kalman filter that employs ROE-based dynamics model as well as first-order accurate measurement model that relates ROEs directly to angle measurements [10]. A sensitivity analysis is performed by closing the loop of the navigation system with a guidance and control law for the chaser spacecraft in a rendezvous scenario. The chaser spacecraft employs a two-point optimal guidance law developed by Chihabi and Ulrich [23] in combination with a Guardian map-based Simple Adaptive Control law [15]. In addition, a comparison with both a maneuvering and a passive target spacecraft is provided. The proposed model was validated in both LEO and HEO.

The numerical propagator used as the truth model integrates the inertial two-body equation of motion to which the inertial perturbing accelerations are added. Specifically, perturbing accelerations due to gravitational field through the expansion of gravitational potential function up to degree and order 180 [24], third body effects of the sun, moon and solar system planets [25,26], ocean and solid Earth tidal effects, relativity [24], solar radiation pressure, and drag are included [27]. This numerical propagator is developed within MATLAB/Simulink environment using the International Astronomical Union's software package for dynamical astronomy, which features the most accurate numerical propagation of spacecraft and celestial bodies. Note that an off-the-shelf propagator, such as NORAD's SGP4, could be used; however, it is only useful for long-term propagation and orbital analysis due to its computational efficiency. Generally, numerical integrators display more accurate orbit propagation when compared to analytical propagators such as SGP4/SDP4. In MATLAB,

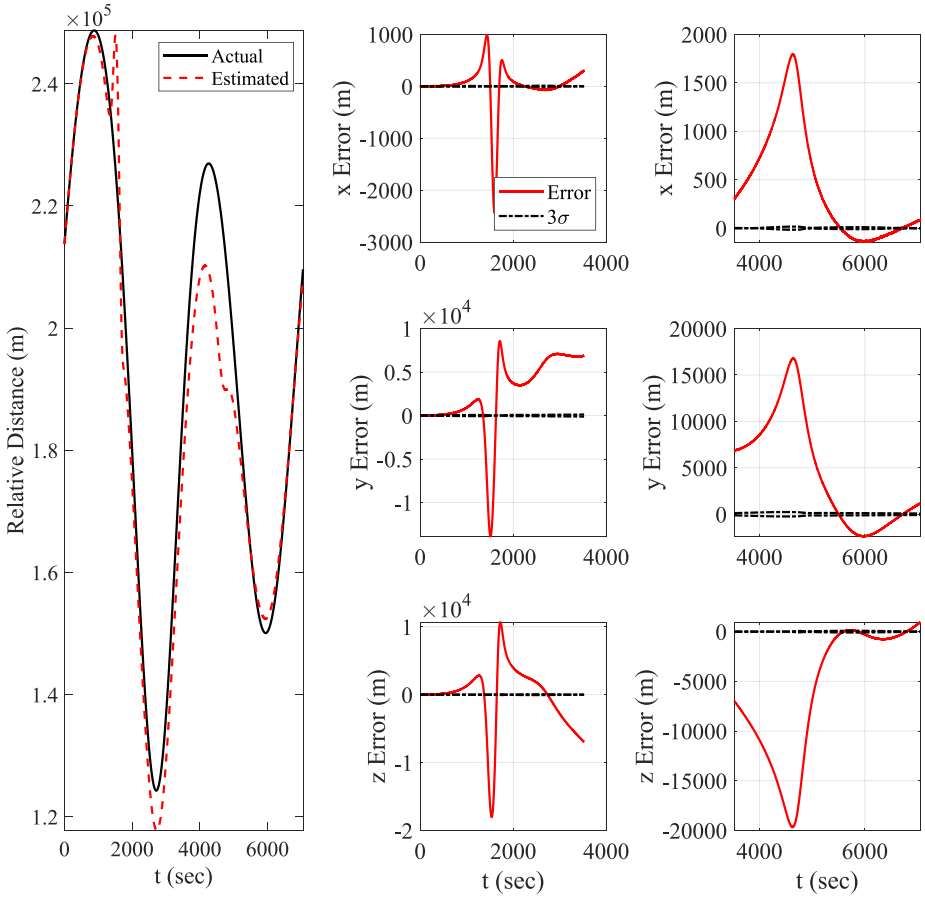

Fig. 3. LEO EKF estimation errors using Hamiltonian dynamics and proposed nonlinear measurement model (without adaptive covariance tuning).

an ODE45 solver with a relative and absolute tolerance of 1×10^{-9} was selected for all cases.

The initial time was selected as July 1, 2014 for Planetary Ephemeris. The mass and cross-sectional area are 211 kg and 1.77 m^2, and 339 kg and 3.34 m^2 for the chaser and target spacecraft, respectively [28]. For the solar radiation pressure model, a constant coefficient of reflectivity of 2 is used for both spacecraft. For all simulation cases, the Kalman filters were initialized with the following values: $\boldsymbol{P}_0 = (1\times10^{-20})\boldsymbol{I}_6$, $\boldsymbol{Q}_0 = (1\times10^{-10})\boldsymbol{I}_6$, $\boldsymbol{R}_0 = (1\times10^{-4})\boldsymbol{I}_3$, $\alpha = 1\times10^{-3}$, $\beta = 2$, $\kappa = 0$, and $N = 60$.

4.1. Low earth orbit

The orbital elements for low Earth orbit is selected as $a_t = 7947$ km, $e_t = 0.1343248$, $i_t = 79.7965°$, $\omega_t = 165.8128°$, $\Omega_t = 261.0864°$, and $\theta_t = 194.2893°$. The initial orbital elements for the chaser were selected such that $\Delta\boldsymbol{x}_0 = \begin{bmatrix}-0.5 & -5\times10^{-4} & -1° & -1° & 1° & -0.2°\end{bmatrix}^T$.

4.1.1. Passive chaser and target

Table 1 shows the 3D RMS results for each filtering strategy, benchmarked against the filtering strategy employed in [10] for a passive chaser and target scenario in LEO. The 3D RMS values for each scenario are calculated as

$$\text{3D-RMS} = \sqrt{\frac{1}{N}\sum_{j=j_0}^{N}\left[\left(x_j-\hat{x}_j\right)^2+\left(y_j-\hat{y}_j\right)^2+\left(z_j-\hat{z}_j\right)^2\right]} \tag{64}$$

Based on the 3D RMS values for each filtering strategy, a steady decrease in error is observed between the reference EKF, the EKF employing the proposed Hamiltonian dynamics with the nonlinear measurement model, and the adaptive EKF, while the adaptive UKF showed the greatest decrease of a whole magnitude in 3D RMS error. These can be verfied through Figs. 2 to 5, which present the relative navigation error results as a function of time. Fig. 2 shows the error for the reference case which employs an extended Kalman filter with ROE based dynamics and first order measurement model. When compared with Fig. 4, which utilizes Hamiltonian dynamics along with exact nonlinear Equations for the measurement model, the improvement in accuracy becomes apparent. As shown in Fig. 4, the errors converge to values closer to 0 in the x and y directions, while being two orders of magnitude lower in the z-direction as opposed to Fig. 2 which diverges about all three axes. Fig. 5 shows the navigation error for the UKF case and when compared with Fig. 4 shows a minor increase in accuracy about all three axes, with the in-plane motion error converging to a value closer to 0.

Table 1
Passive chaser and target average RMS error.

Method	3D position RMS error (m)
Benchmark EKF [10]	22 883.8
EKF, Proposed dynamics and measurement models	19 473.3
Adaptive EKF	15 381.1
Adaptive UKF	3458.1

Histograms of the error distributions are also provided in Figs. 6 and 7. The improvement the Hamiltonian dynamics and nonlinear measurement model has over the benchmark EKF is clear in Fig. 6, which shows that near-zero error are over two times as frequent when comparing proposed dynamics and measurement models with the reference EKF. Furthermore, when comparing the adaptive UKF

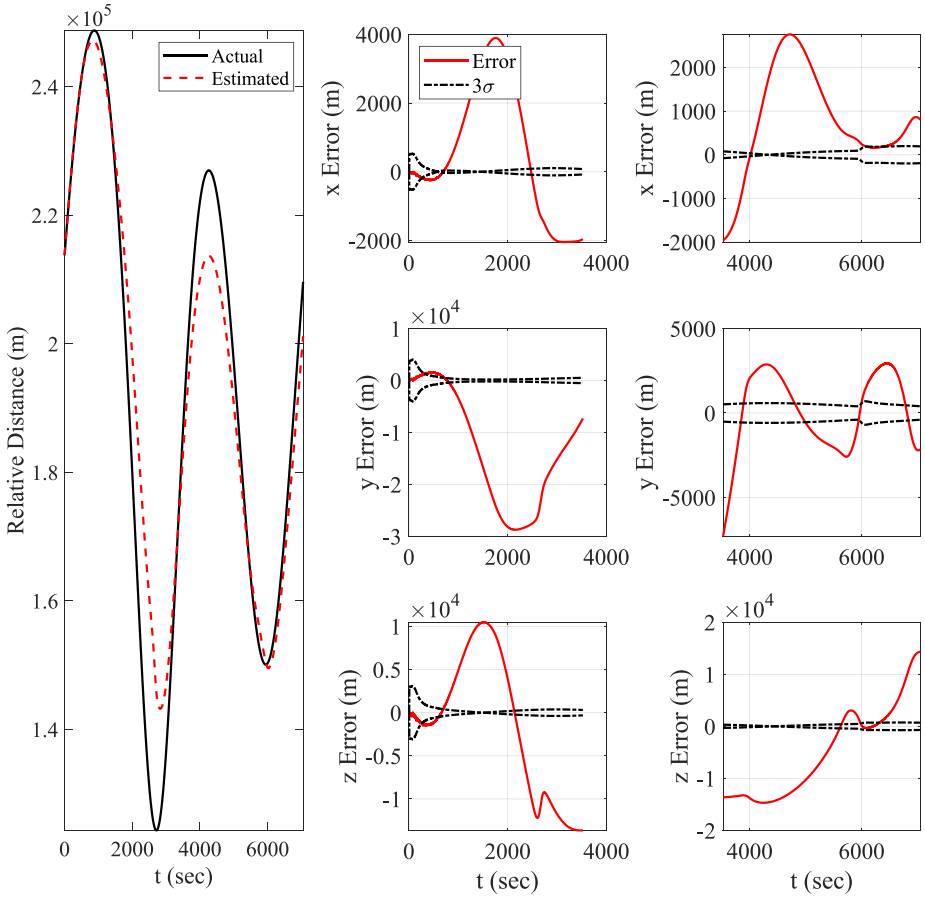

Fig. 4. LEO EKF estimation errors using Hamiltonian dynamics and proposed nonlinear measurement model (with adaptive covariance tuning).

Table 2
Maneuvering chaser and passive target average RMS error.

Method	3D position RMS error (m)
Adaptive EKF	11 167.5
Adaptive UKF	3295.5

Table 3
Maneuvering chaser and target average RMS error.

Method	3D position RMS error (m)
Adaptive EKF	11 176.3
Adaptive UKF	3297.4

with the adaptive EKF in Fig. 7, the estimation accuracies for the UKF are considerably greater. This is due to the nonlinear nature of the UKF which allows for the filtering algorithm to take full advantage of the nonlinear measurement model and Hamiltonian dynamics, which otherwise are linearized by the EKF.

4.1.2. Maneuvering chaser and passive target

Figs. 8 and 9 show the results for a maneuvering chaser rendezvous with a passive target spacecraft. Table 2 similarly shows the 3D RMS errors for the adaptive UKF and adaptive EKF. The errors are considerably larger for the EKF case, especially along the y and z directions by an order of magnitude, and the UKF converges closer to 0 and maintains accurate relative distance estimation as opposed to the EKF case. When comparing these results with the passive case from the previous section, it becomes apparent that the UKF is more robust to the chaser's control maneuvers than the EKF. This can be seen when observing the 3D RMS errors, which shows an order of magnitude improvement in accuracy for the adaptive UKF case.

The superiority of the adaptive UKF can again be seen with the provided histogram of the error distributions in Fig. 10. Specifically, the estimation errors for the adaptive UKF are more concentrated close towards the zero meter error mark, while the adaptive EKF clearly shows more frequent errors of greater than 5000 m. Furthermore, this is especially true for the in-plane motion, where the adaptive EKF eventually diverges from the true solution as depicted in the previous error graphs.

4.1.3. Maneuvering chaser and target

Figs. 11 and 12 show the results for a scenario where both the target and chaser are maneuvering. The target's maneuvers are applied using a random number generator with a mean of 0 and a variance of 1×10^{-4}. Similar to the previous case where only the chaser is maneuvering, the UKF maintains a higher accuracy than the EKF. Furthermore, when comparing the results of this case with the previous case, the errors show negligible difference in accuracy due to the adaptive MLE with intrinsic smoothing accounting for the target's maneuvers within the covariance matrices. The corresponding 3D RMS results and histogram are provided in Table 3 and Fig. 13, respectively.

4.2. Highly elliptical orbit

The initial osculating orbital elements for the highly elliptical orbit example were initialized as a_t = 40000 km, e_t = 0.8325, i_t = 90.0°, ω_t = 350°, Ω_t = 100.0°, and θ_t = 180°. The initial ROE, $\Delta\boldsymbol{x}_0$, is equivalent to the one selected for the LEO case with the same scenario duration.

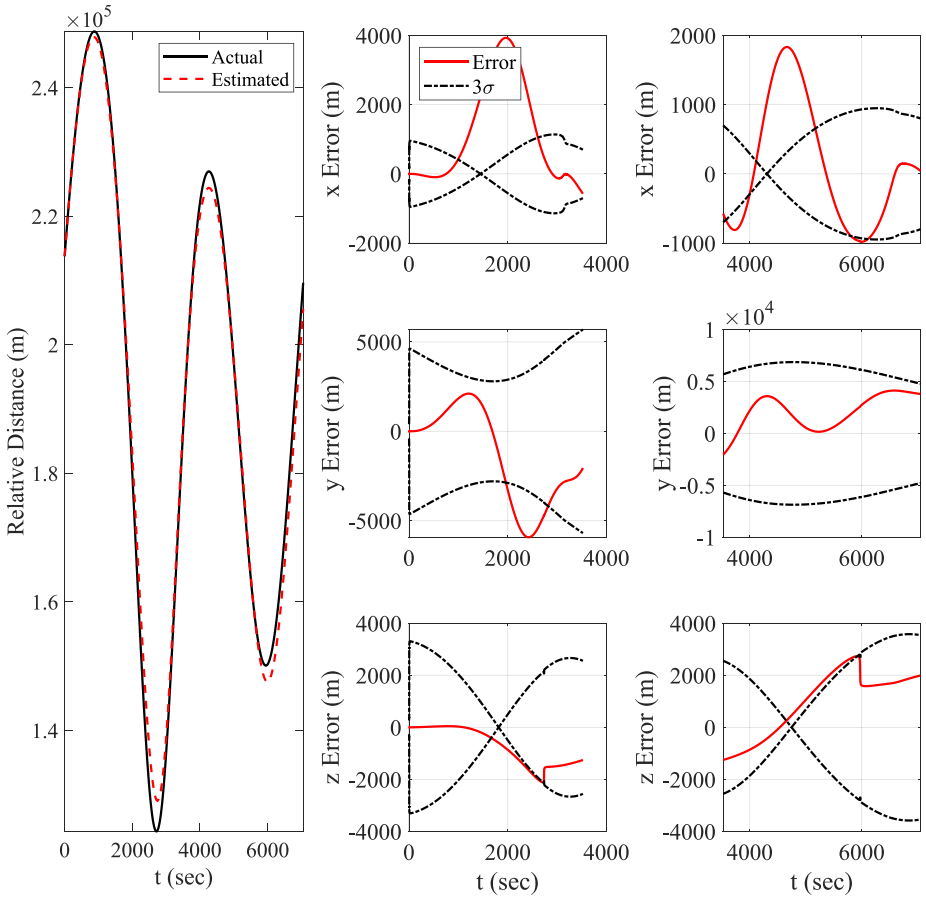

Fig. 5. LEO UKF estimation errors using Hamiltonian dynamics and proposed nonlinear measurement model.

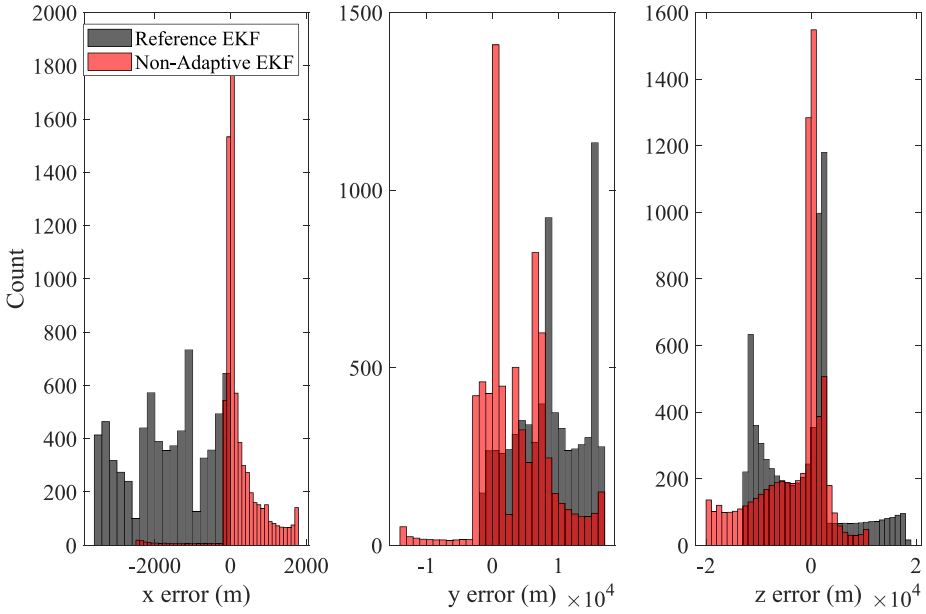

Fig. 6. LEO relative position error distributions for reference ROE based EKF and non-adaptive EKF with proposed dynamics and measurement model.

4.2.1. Passive chaser and target

Similarly to the LEO example, Table 4 shows the 3D RMS results for each filtering strategy, benchmarked against the filtering strategy employed in [10] for a passive chaser and target scenario, this time, applied in HEO. Figs. 14 to 17 present the relative navigation error results for a passive chaser and target scenario. The errors for Fig. 15 the errors converge to values closer to 0 in the x and y directions, while peak errors reduced by half for all three axes as opposed to Fig. 14. Fig. 16 shows the results for the EKF except with the adaptive algorithm enabled. Enabling the adaptation law results in more accurate estimates for relative motion mid-way through the simulation period, during which the spacecraft are approaching

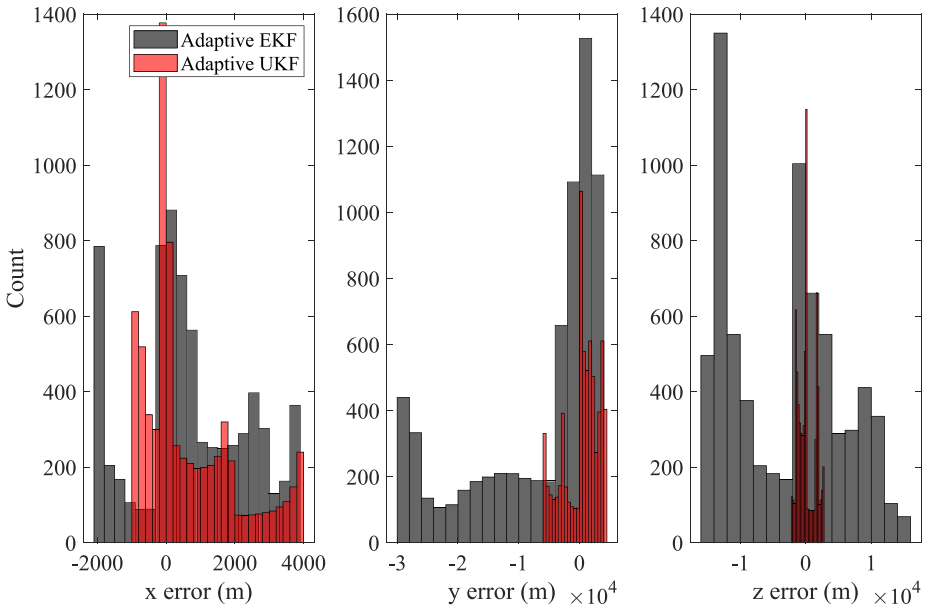

Fig. 7. LEO relative position error distributions for adaptive EKF and UKF.

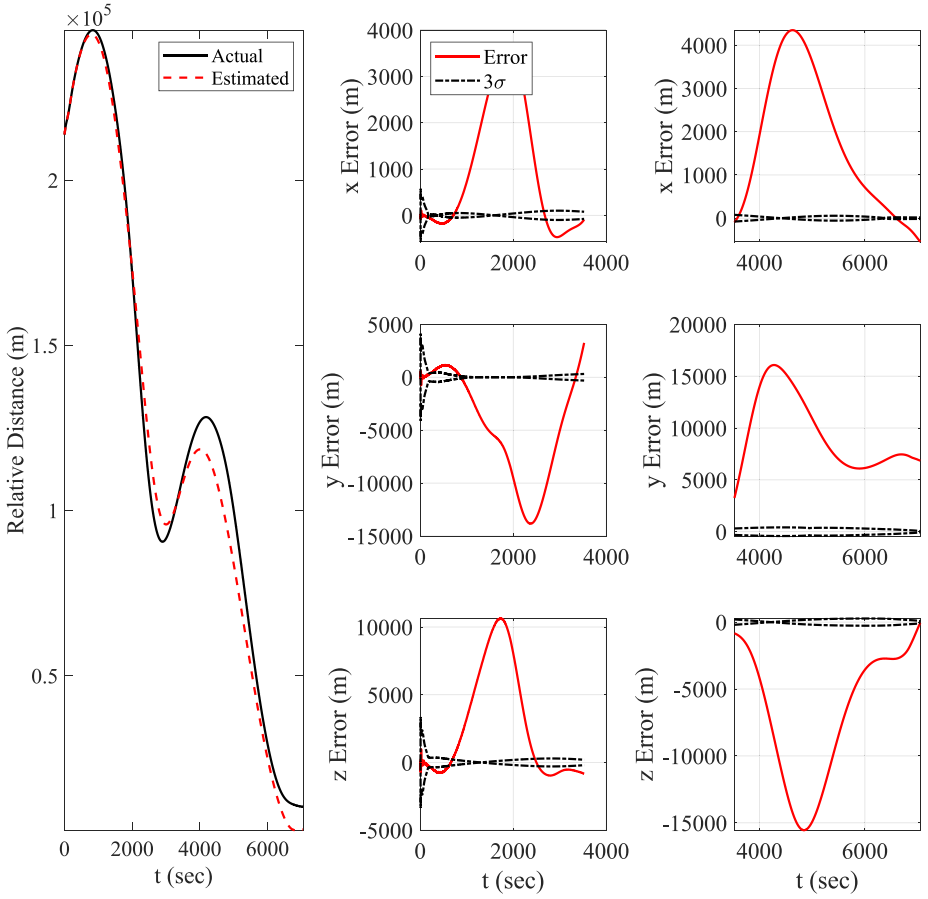

Fig. 8. LEO EKF estimation errors using Hamiltonian dynamics and proposed nonlinear measurement models.

perigee. Fig. 17 shows the navigation error for the UKF case and when compared with Fig. 15 shows a major increase in accuracy about all three axes, with the in-plane motion error converging closer to 0. These conclusions are reflected when observing the accompanying histograms in Figs. 18 and 19. The results for the HEO passive case, when comparing to the LEO passive case, demonstrate the robustness of both the UKF and the adaptation algorithm to the variation in the orbital regime since they resulted in a more significant increase in relative navigation accuracy in the HEO case as opposed to the LEO case.

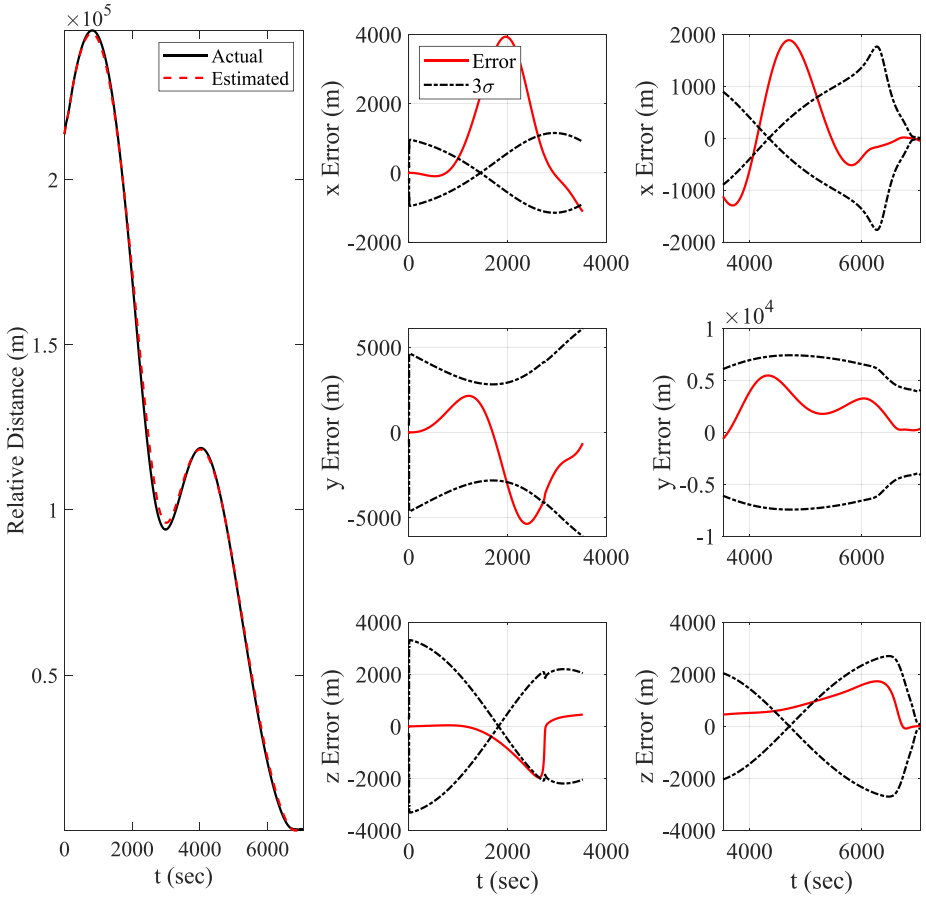

Fig. 9. LEO UKF estimation errors using Hamiltonian dynamics and proposed nonlinear measurement models.

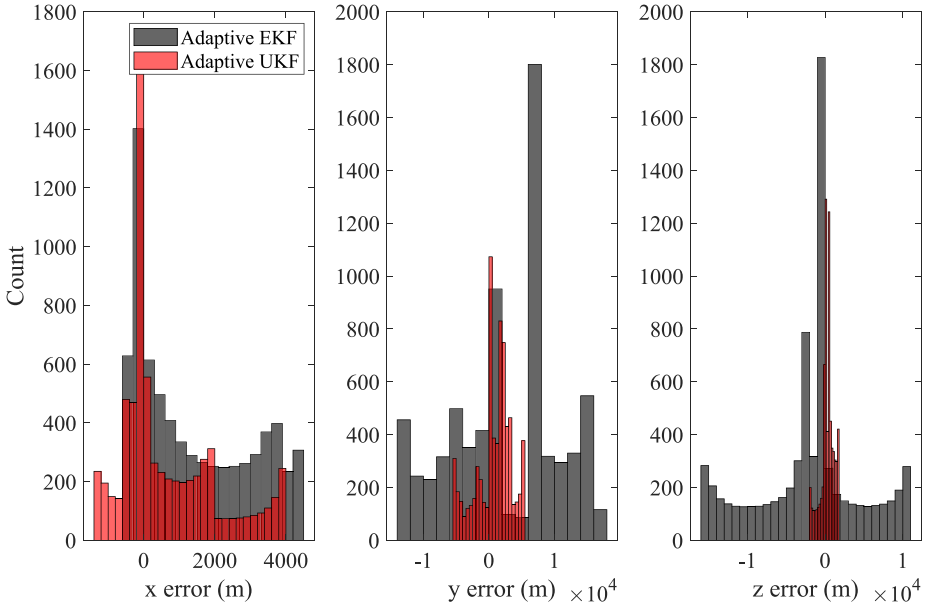

Fig. 10. LEO relative position error distributions for adaptive EKF and UKF.

4.2.2. *Maneuvering chaser and passive target*

Table 5 similarly shows the 3D RMS errors for the adaptive UKF and adaptive EKF, except this time for a chaser spacecraft rendezvous with a passive target in HEO. Figs. 20 and 21 show the errors as a function of time. The errors are considerably larger for the EKF case, especially along the y and z directions by an order of magnitude, and the UKF converges closer to 0 and maintains accurate relative distance estimation as opposed to the EKF case. As expected, the relative navigation errors follow the same trend as the LEO case with the maneuvering chaser. However, the relative navigation error towards the end of the scenario is much larger for the EKF in the HEO case than in the LEO case. This is due to the fact that the EKF algorithm employs a

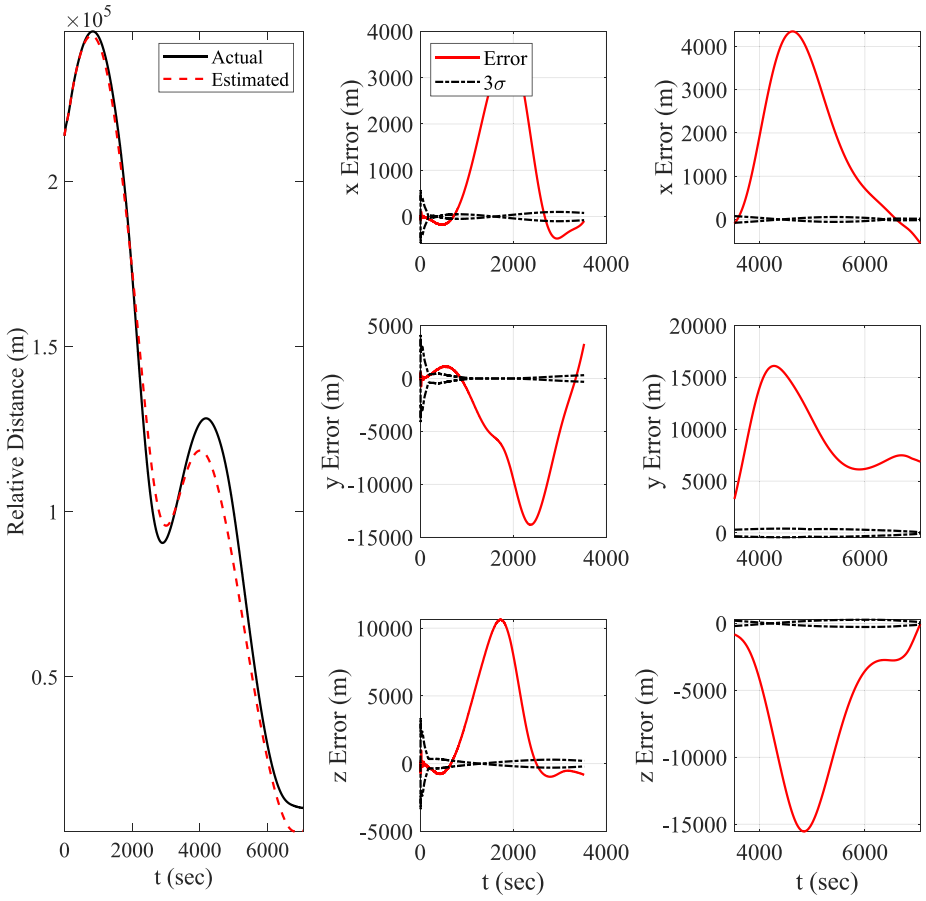

Fig. 11. LEO EKF estimation errors using Hamiltonian dynamics and proposed nonlinear measurement models.

Table 4
Passive chaser and target average RMS error.

Method	3D position RMS error (m)
Benchmark EKF [10]	86 698.2
EKF, proposed dynamics and measurement models	82 447.5
Adaptive EKF	79 175.2
Adaptive UKF	31 516.3

Table 5
Maneuvering chaser and passive target average RMS error.

Method	3D position RMS error (m)
Adaptive EKF	78 166.2
Adaptive UKF	23 258.4

linearization process as opposed to the UKF which is a nonlinear algorithm capable of capturing nonlinearities that are inherent in highly elliptical orbits.

Similar to the LEO case, the superiority of the adaptive UKF can again be seen with the provided histogram of the error distributions in Fig. 22. Specifically, the estimation errors for the adaptive UKF are more concentrated close towards the zero meter error mark, while the adaptive EKF clearly shows more frequent errors of greater than 5000 m. Furthermore, this is especially true for the in-plane motion, where the adaptive EKF eventually diverges from the true solution as depicted in the previous error graphs.

Table 6
Maneuvering chaser and target average RMS error.

Method	3D position RMS error (m)
Adaptive EKF	78 272.8
Adaptive UKF	23 348.7

4.2.3. Maneuvering chaser and target

Figs. 23 and 24 show the results for a scenario where both the target and chaser are maneuvering. The target's maneuvers are applied using a random number generator with a mean of 0 and a variance of 1×10^{-4}, similar to the LEO case. Similar to the previous case where only the chaser is maneuvering, the UKF maintains a higher accuracy than the EKF. Furthermore, when comparing the results of this case with the previous case, the errors show negligible difference in accuracy due to the adaptive MLE with intrinsic smoothing accounting for the target's maneuvers within the covariance matrices. The corresponding 3D RMS results and histogram are provided in Table 6 and Fig. 25, respectively.

5. Conclusion

This work presented an adaptive angle-only navigation solution using both the extended and the unscented Kalman filters for spacecraft relative motion. The proposed method utilized Hamiltonian dynamics while considering the effects of J_2, luni-solar perturbations, solar radiation pressure and atmospheric drag complete with their peri-

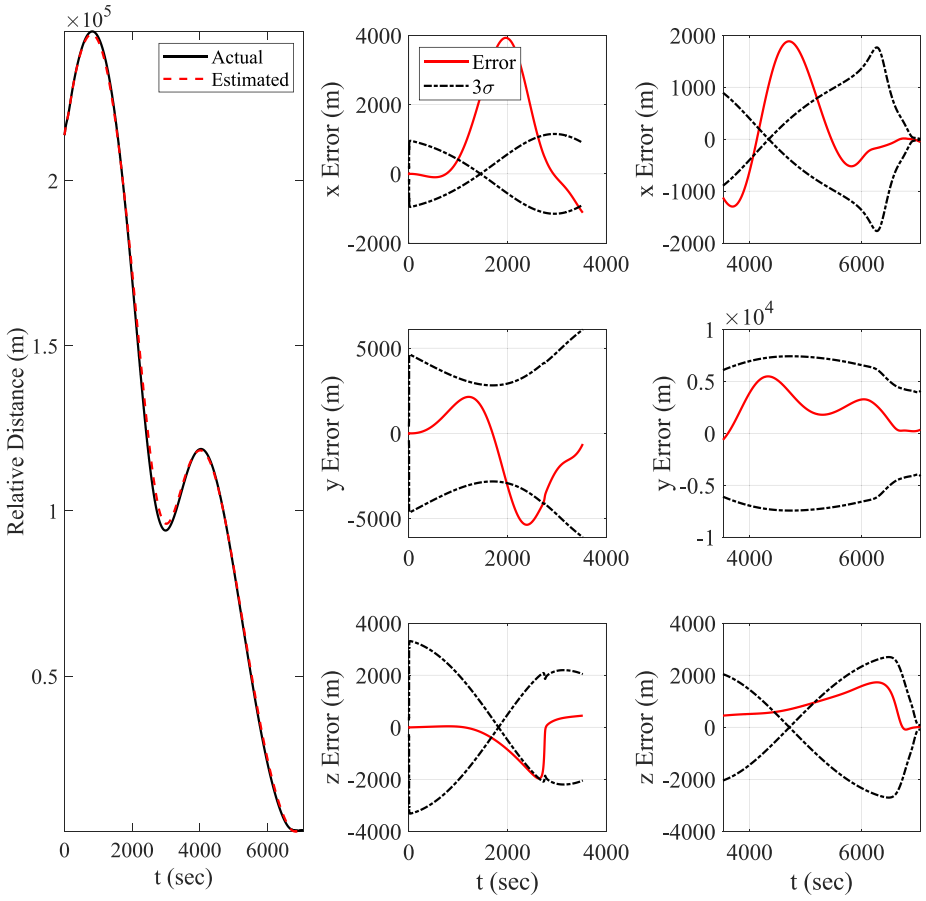

Fig. 12. LEO UKF estimation errors using Hamiltonian dynamics and proposed nonlinear measurement models.

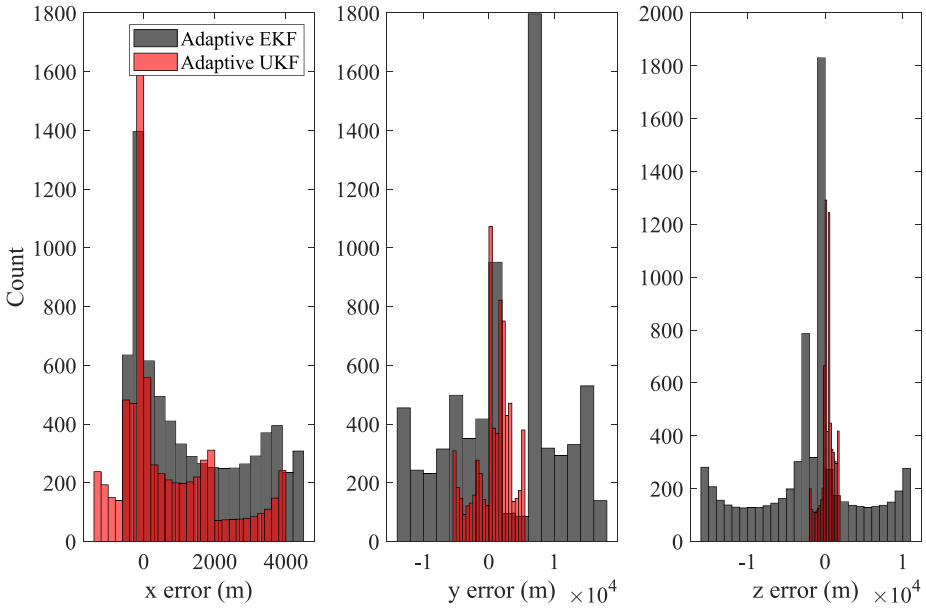

Fig. 13. LEO relative position error distributions for adaptive EKF and UKF.

odic variations. A novel measurement model that exactly maps orbital elements to angle measurements was derived that by-passes the first-order limitations of previous the measurement model used in literature. In addition, the adaptive algorithm incorporated the use of intrinsic smoothing with maximum likelihood estimation to tune the covariance matrices of the Kalman filters on-line.

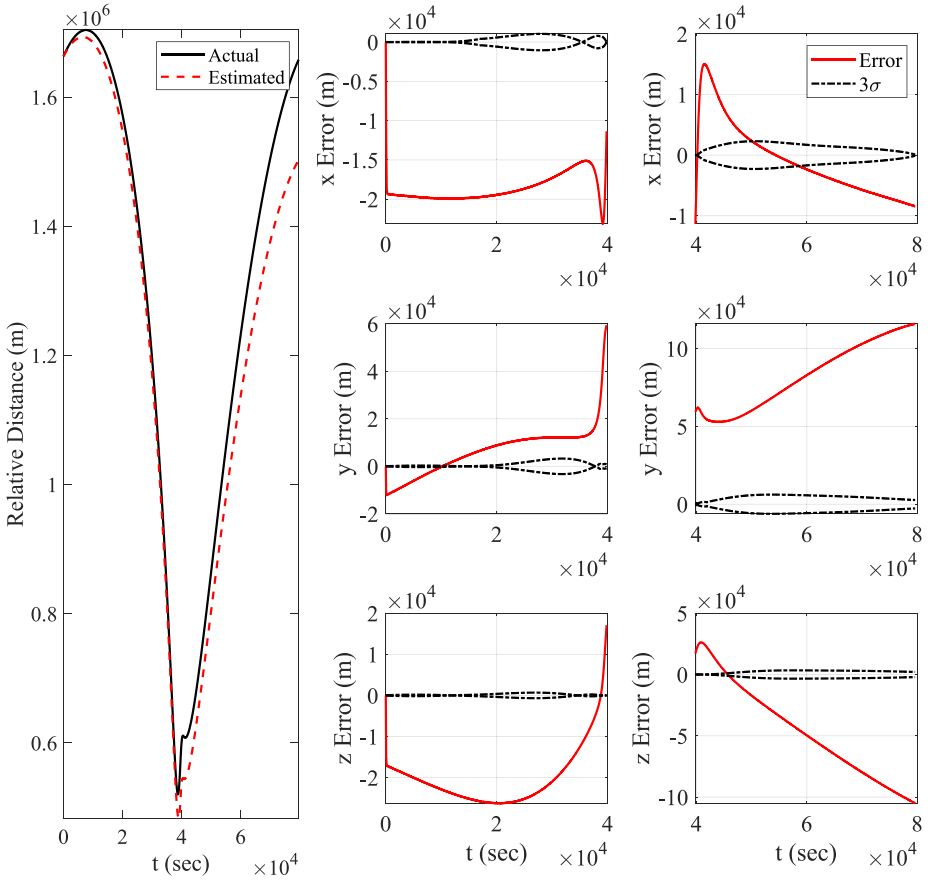

Fig. 14. HEO EKF estimation errors using ROE dynamics and measurement models.

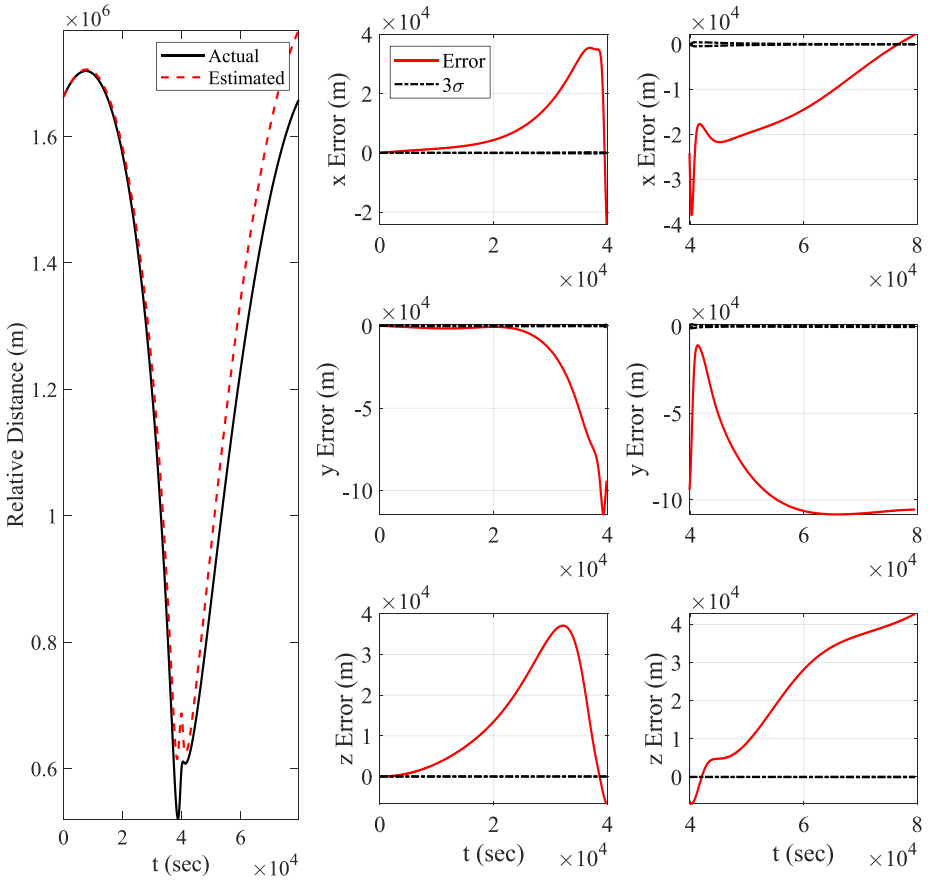

Fig. 15. HEO EKF estimation errors using Hamiltonian dynamics and proposed nonlinear measurement models (without adaptive covariance tuning).

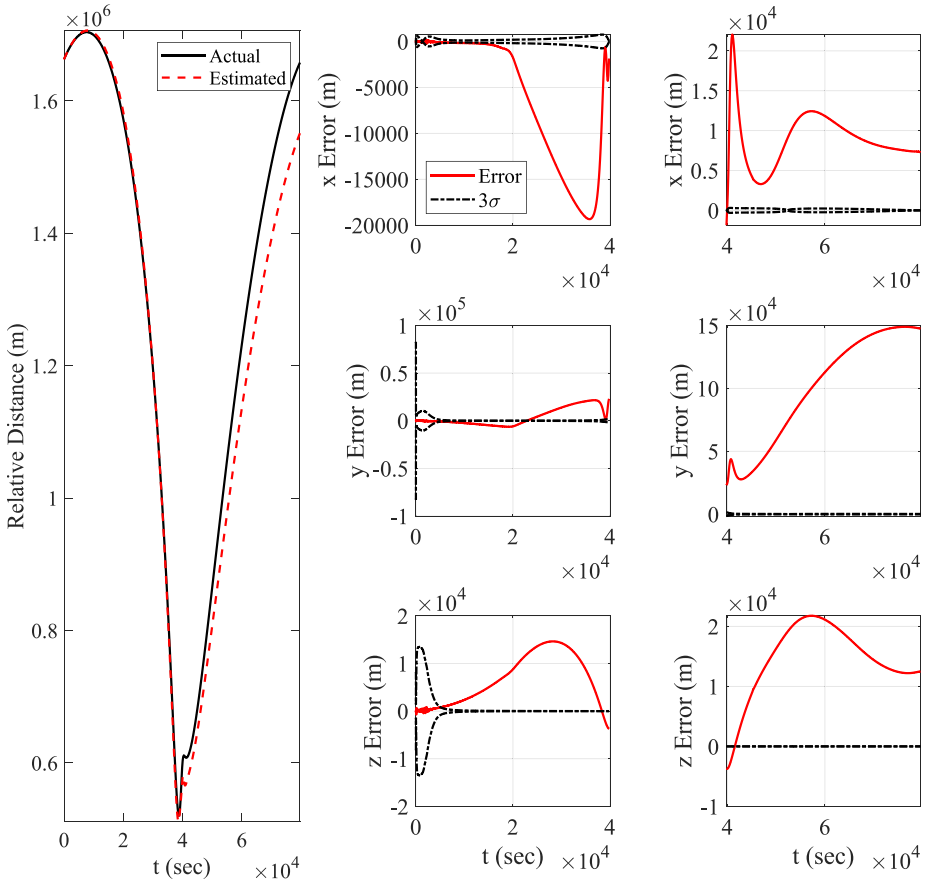

Fig. 16. HEO EKF estimation errors using Hamiltonian dynamics and proposed nonlinear measurement models (with adaptive covariance tuning).

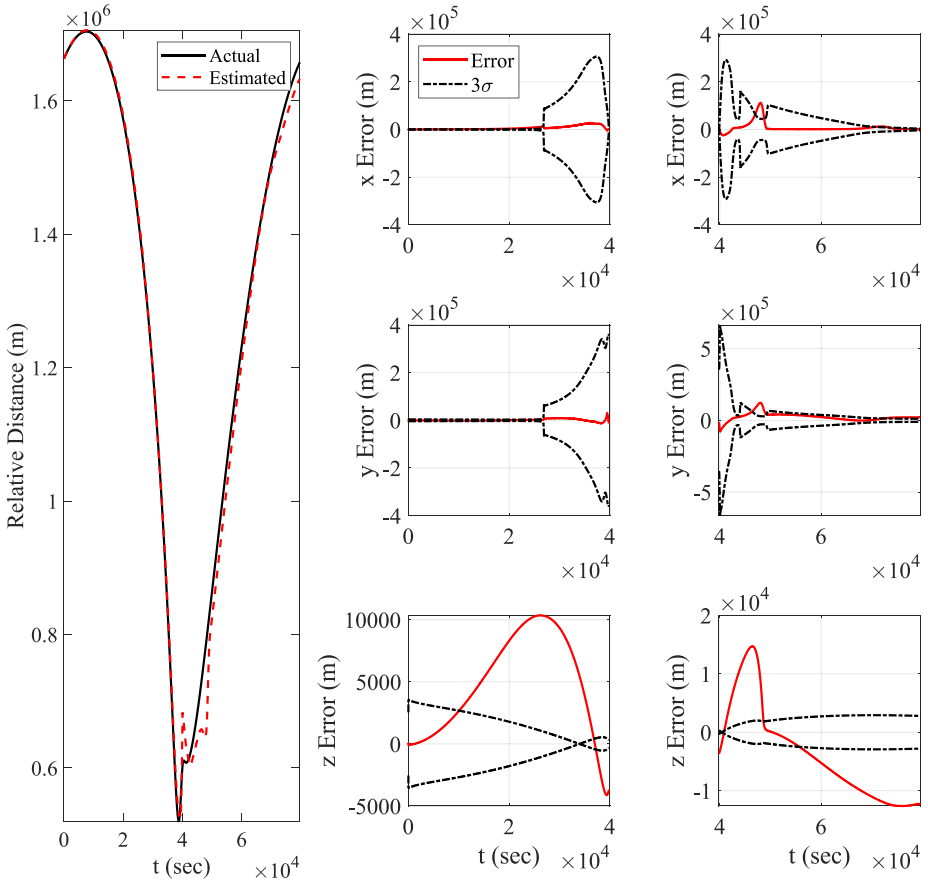

Fig. 17. HEO UKF estimation errors using Hamiltonian dynamics and proposed nonlinear measurement models (with adaptive covariance tuning).

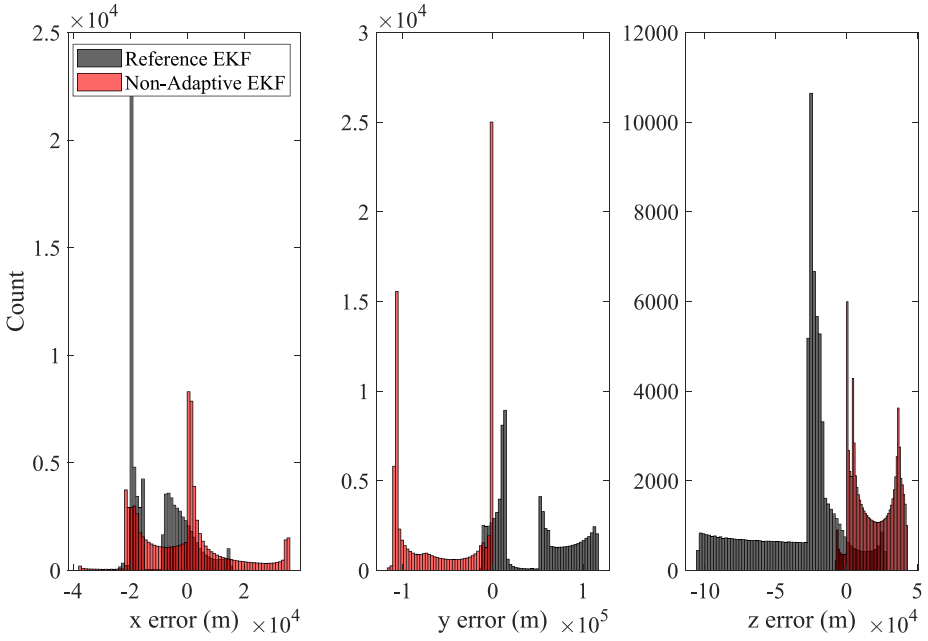

Fig. 18. HEO relative position error distributions for reference ROE based EKF and non-adaptive EKF with proposed measurement model.

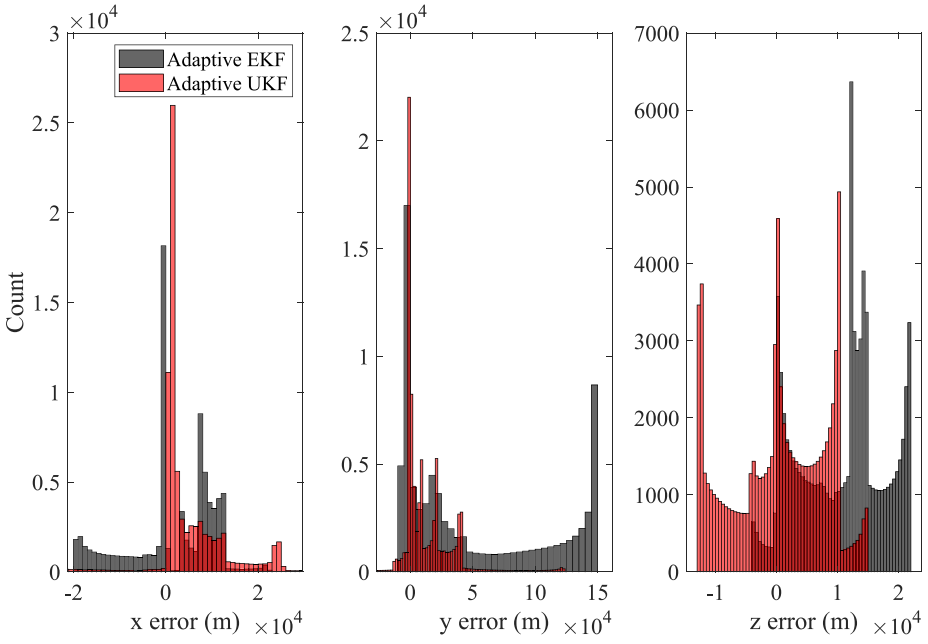

Fig. 19. HEO relative position error distributions for adaptive EKF and UKF.

Two formation flying scenarios, one on a highly elliptical reference orbit and the other in low earth orbit, were tested in simulation for various passive and maneuvering spacecraft cases. The results showed the effectiveness of the proposed measurement and process models over the relative orbital elements based models, where the proposed model resulted in orders of magnitude decrease in estimation errors. Furthermore, the adaptive algorithm and unscented Kalman filter demonstrated a higher accuracy in the highly elliptical reference orbit case than the low Earth orbit due to the fact that nonlinearities increase drastically as the eccentricity of the orbit increases. Future work will be done to incorporate a method to estimate the target control inputs to further improve the estimation accuracy.

Declaration of competing interest

The authors declare that they have no known competing financial interests or personal relationships that could have appeared to influence the work reported in this paper.

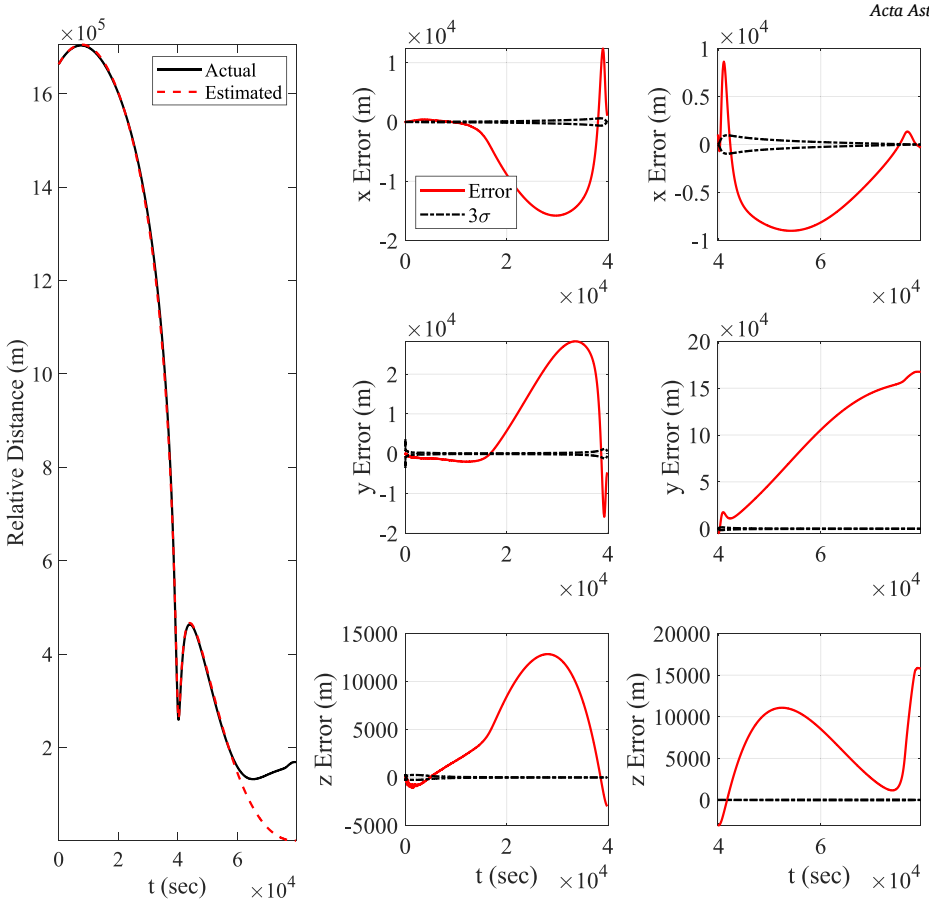

Fig. 20. HEO EKF estimation errors using Hamiltonian dynamics and proposed nonlinear measurement models (with adaptive covariance tuning).

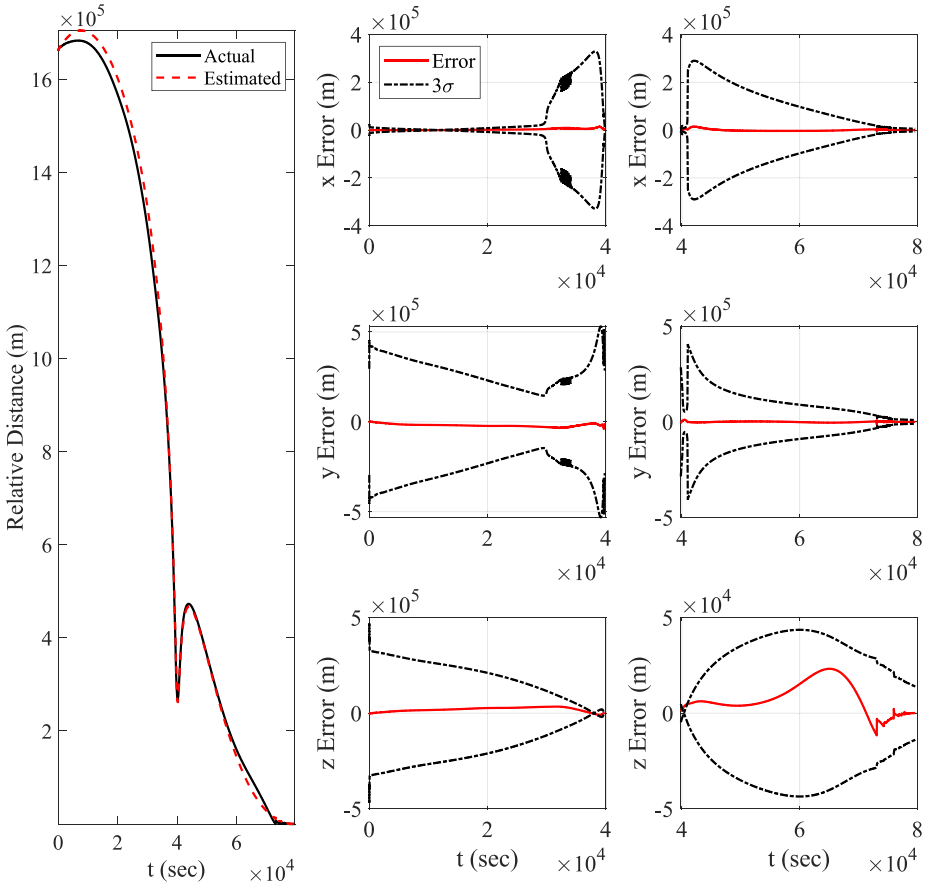

Fig. 21. HEO UKF estimation errors using Hamiltonian dynamics and proposed nonlinear measurement models (with adaptive covariance tuning).

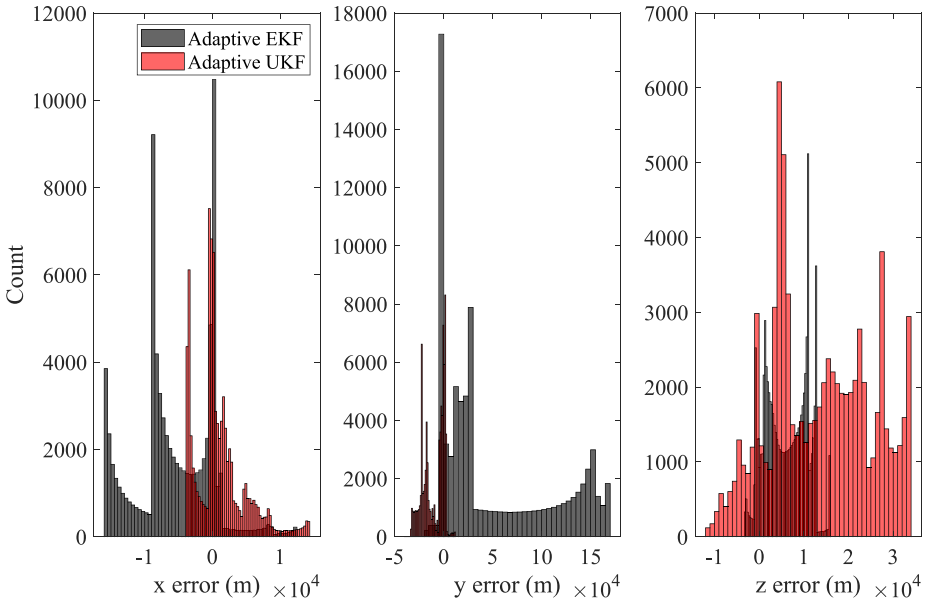

Fig. 22. HEO relative position error distributions for adaptive EKF and UKF.

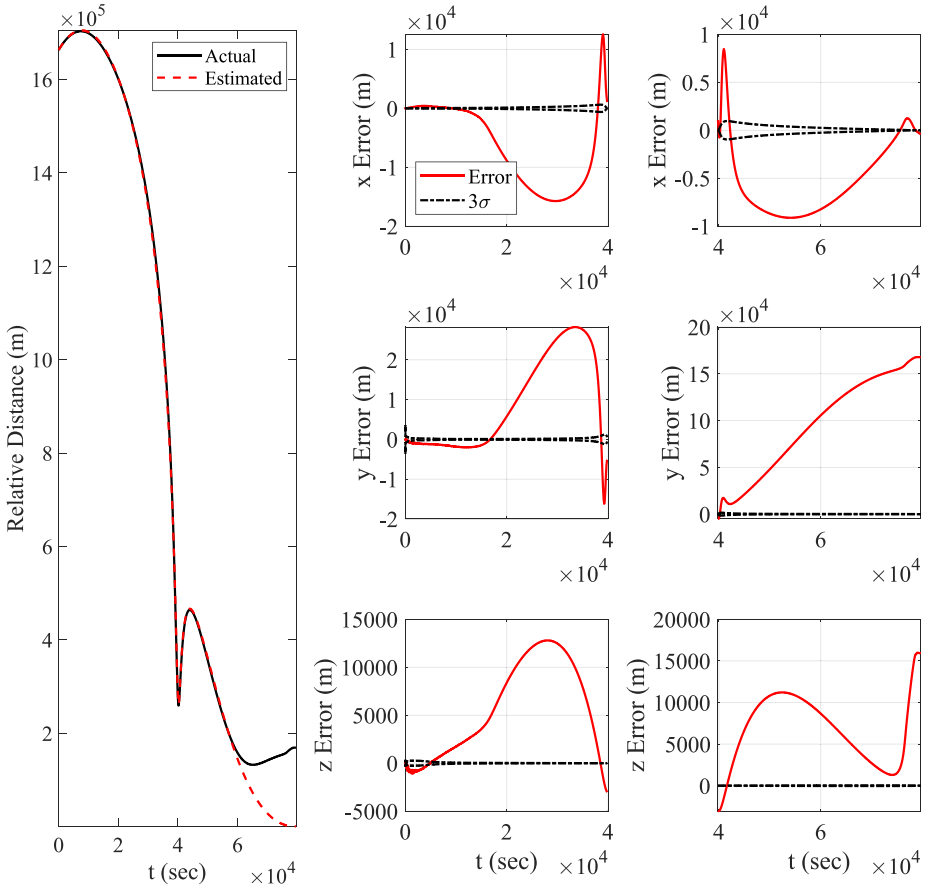

Fig. 23. HEO EKF estimation errors using Hamiltonian dynamics and proposed nonlinear measurement models (with adaptive covariance tuning).

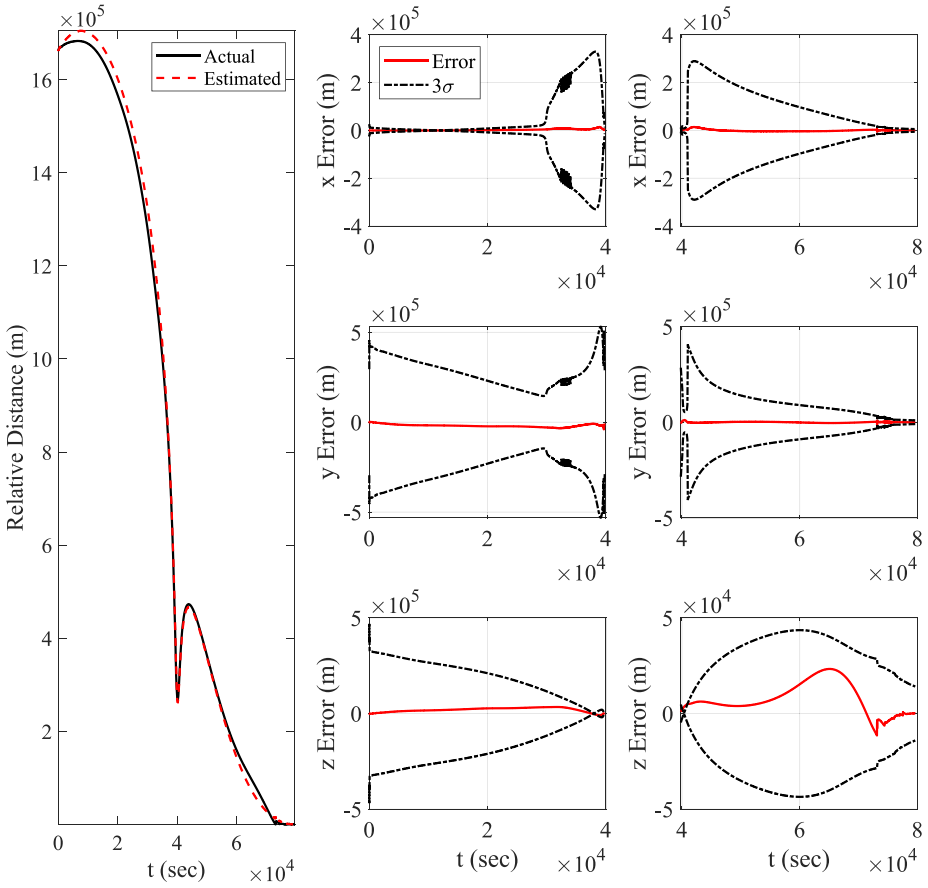

Fig. 24. HEO UKF estimation errors using Hamiltonian dynamics and proposed nonlinear measurement models (with adaptive covariance tuning).

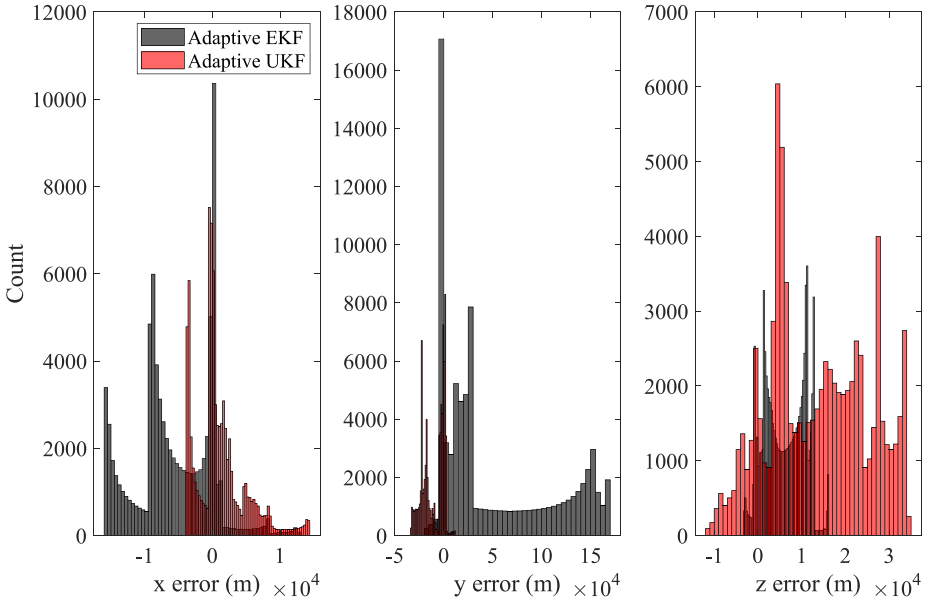

Fig. 25. HEO relative position error distributions for adaptive EKF and UKF.

Appendix A. Partial derivatives

This appendix presents the partial derivatives used in the derivation of the navigation algorithms proposed in this paper.

$$\frac{\partial M}{\partial \theta} = \frac{\left(1-e^2\right)^{3/2}}{(e\cos(\theta)+1)^2} \tag{A.1}$$

$$\frac{\partial r}{\partial a} = -\frac{e^2-1}{e\cos(\theta)+1} \tag{A.2}$$

$$\frac{\partial r}{\partial e} = \frac{a\cos(\theta)\left(e^2-1\right)}{(e\cos(\theta)+1)^2} - \frac{2ae}{e\cos(\theta)+1} \tag{A.3}$$

$$\frac{\partial r}{\partial \theta} = -\frac{ae\sin(\theta)\left(e^2-1\right)}{(e\cos(\theta)+1)^2} \tag{A.4}$$

$$\frac{\partial}{\partial i}\boldsymbol{C}_{IP}(\omega,i,\Omega) = \begin{bmatrix} s_\Omega s_\omega s_i & s_\Omega c_\omega s_i & s_\Omega c_i \\ -c_\Omega s_\omega s_i & -c_\Omega c_\omega s_i & c_\Omega c_i \\ s_\omega c_i & c_\omega c_i & -s_i \end{bmatrix} \tag{A.5}$$

$$\frac{\partial}{\partial \omega}\boldsymbol{C}_{IP}(\omega,i,\Omega) = \begin{bmatrix} -c_\Omega s_\omega - s_\Omega c_\omega c_i & -c_\Omega c_\omega + s_\Omega s_\omega c_i & 0 \\ -s_\Omega s_\omega + c_\Omega c_\omega c_i & -s_\Omega c_\omega + c_\Omega s_\omega c_i & 0 \\ c_\omega s_i & -s_\omega s_i & 0 \end{bmatrix} \tag{A.6}$$

$$\frac{\partial}{\partial \Omega}\boldsymbol{C}_{IP}(\omega,i,\Omega) = \begin{bmatrix} -s_\Omega c_\omega - c_\Omega s_\omega c_i & s_\Omega s_\omega - c_\Omega c_\omega c_i & c_\Omega s_i \\ c_\Omega c_\omega - s_\Omega s_\omega c_i & -c_\Omega s_\omega + s_\Omega c_\omega c_i & s_\Omega s_i \\ 0 & 0 & 0 \end{bmatrix} \tag{A.7}$$

$$\frac{\partial}{\partial \theta}\boldsymbol{C}_{LP}(\theta) = \begin{bmatrix} -s_\theta & c_\theta & 0 \\ -c_\theta & -s_\theta & 0 \\ 0 & 0 & 1 \end{bmatrix} \tag{A.8}$$

Appendix B. Partial derivatives of measurement model matrix

This appendix provides the MATLAB symbolic derivation of the partial derivatives used in the measurement model matrix.

$$\begin{aligned} H^2_{nu,1} = & -2\left(\frac{{p_c}^2 c_{\theta_c} s_{i_c} s_{\omega_c}}{a_c r_c} + \frac{{p_c}^2 c_{\omega_c} s_{i_c} s_{\theta_c}}{a_c r_c}\right)\left(\frac{{p_c}^2 c_{\theta_c} s_{i_c} s_{\omega_c}}{r_c} \right. \\ & \left. + \frac{{p_c}^2 c_{\omega_c} s_{i_c} s_{\theta_c}}{r_c} - \frac{{p_t}^2 c_{\theta_t} s_{i_t} s_{\omega_t}}{r_t} - \frac{{p_t}^2 c_{\omega_t} s_{i_t} s_{\theta_t}}{r_t}\right) \\ & + 2\left(\frac{{p_c}^2 c_{\theta_c}\left(s_{\Omega_c} c_{\omega_c} + c_{\Omega_c} c_{i_c} s_{\omega_c}\right)}{a_c r_c} - \frac{{p_c}^2 s_{\theta_c}\left(s_{\Omega_c} s_{\omega_c} - c_{\Omega_c} c_{i_c} c_{\omega_c}\right)}{a_c r_c}\right)\times \\ & \left(\frac{{p_c}^2 c_{\theta_c}\left(s_{\Omega_c} c_{\omega_c} + c_{\Omega_c} c_{i_c} s_{\omega_c}\right)}{r_c} - \frac{{p_t}^2 c_{\theta_t}\left(s_{\Omega_t} c_{\omega_t} + c_{\Omega_t} c_{i_t} s_{\omega_t}\right)}{r_t} \right. \\ & \left. - \frac{{p_c}^2 s_{\theta_c}\left(s_{\Omega_c} s_{\omega_c} - c_{\Omega_c} c_{i_c} c_{\omega_c}\right)}{r_c} + \frac{{p_t}^2 s_{\theta_t}\left(s_{\Omega_t} s_{\omega_t} - c_{\Omega_t} c_{i_t} c_{\omega_t}\right)}{r_t}\right) \\ & + 2\left(\frac{{p_c}^2 c_{\theta_c}\left(c_{\Omega_c} c_{\omega_c} - s_{\Omega_c} c_{i_c} s_{\omega_c}\right)}{a_c r_c} - \frac{{p_c}^2 s_{\theta_c}\left(c_{\Omega_c} s_{\omega_c} + s_{\Omega_c} c_{i_c} c_{\omega_c}\right)}{a_c r_c}\right)\times \\ & \left(\frac{{p_c}^2 c_{\theta_c}\left(c_{\Omega_c} c_{\omega_c} - s_{\Omega_c} c_{i_c} s_{\omega_c}\right)}{r_c} - \frac{{p_t}^2 c_{\theta_t}\left(c_{\Omega_t} c_{\omega_t} - s_{\Omega_t} c_{i_t} s_{\omega_t}\right)}{r_t} \right. \\ & \left. - \frac{{p_c}^2 s_{\theta_c}\left(c_{\Omega_c} s_{\omega_c} + s_{\Omega_c} c_{i_c} c_{\omega_c}\right)}{r_c} + \frac{{p_t}^2 s_{\theta_t}\left(c_{\Omega_t} s_{\omega_t} + s_{\Omega_t} c_{i_t} c_{\omega_t}\right)}{r_t}\right) \end{aligned} \tag{B.1}$$

$$\begin{aligned} H^2_{de,1} = & 2\left(\left(\frac{{p_c}^2 c_{\theta_c} s_{i_c} s_{\omega_c}}{r_c} + \frac{{p_c}^2 c_{\omega_c} s_{i_c} s_{\theta_c}}{r_c} - \frac{{p_t}^2 c_{\theta_t} s_{i_t} s_{\omega_t}}{r_t} - \frac{{p_t}^2 c_{\omega_t} s_{i_t} s_{\theta_t}}{r_t}\right)^2 \right. \\ & + \left(\frac{{p_c}^2 c_{\theta_c}\left(s_{\Omega_c} c_{\omega_c} + c_{\Omega_c} c_{i_c} s_{\omega_c}\right)}{r_c} - \frac{{p_t}^2 c_{\theta_t}\left(s_{\Omega_t} c_{\omega_t} + c_{\Omega_t} c_{i_t} s_{\omega_t}\right)}{r_t} \right. \\ & \left. - \frac{{p_c}^2 s_{\theta_c}\left(s_{\Omega_c} s_{\omega_c} - c_{\Omega_c} c_{i_c} c_{\omega_c}\right)}{r_c} + \frac{{p_t}^2 s_{\theta_t}\left(s_{\Omega_t} s_{\omega_t} - c_{\Omega_t} c_{i_t} c_{\omega_t}\right)}{r_t}\right)^2 \\ & + \left(\frac{{p_c}^2 c_{\theta_c}\left(c_{\Omega_c} c_{\omega_c} - s_{\Omega_c} c_{i_c} s_{\omega_c}\right)}{r_c} - \frac{{p_t}^2 c_{\theta_t}\left(c_{\Omega_t} c_{\omega_t} - s_{\Omega_t} c_{i_t} s_{\omega_t}\right)}{r_t} \right. \\ & \left. \left. - \frac{{p_c}^2 s_{\theta_c}\left(c_{\Omega_c} s_{\omega_c} + s_{\Omega_c} c_{i_c} c_{\omega_c}\right)}{r_c} + \frac{{p_t}^2 s_{\theta_t}\left(c_{\Omega_t} s_{\omega_t} + s_{\Omega_t} c_{i_t} c_{\omega_t}\right)}{r_t}\right)^2\right)^{3/2} \end{aligned} \tag{B.2}$$

$$\begin{aligned} H^2_{nu,2} = & \frac{2p_c}{{r_c}^2}\left(c_{\theta_c}{p_c}^2 + 2a_c e_c r_c\right)\left(s_{\Omega_c} c_{\theta_c} c_{\omega_c} - s_{\Omega_c} s_{\theta_c} s_{\omega_c} + c_{\Omega_c} c_{i_c} c_{\theta_c} s_{\omega_c} \right. \\ & \left. + c_{\Omega_c} c_{i_c} c_{\omega_c} s_{\theta_c}\right)\left(\frac{{p_c}^2 c_{\theta_c}\left(s_{\Omega_c} c_{\omega_c} + c_{\Omega_c} c_{i_c} s_{\omega_c}\right)}{r_c} \right. \\ & - \frac{{p_t}^2 c_{\theta_t}\left(s_{\Omega_t} c_{\omega_t} + c_{\Omega_t} c_{i_t} s_{\omega_t}\right)}{r_t} - \frac{{p_c}^2 s_{\theta_c}\left(s_{\Omega_c} s_{\omega_c} - c_{\Omega_c} c_{i_c} c_{\omega_c}\right)}{r_c} \\ & \left. + \frac{{p_t}^2 s_{\theta_t}\left(s_{\Omega_t} s_{\omega_t} - c_{\Omega_t} c_{i_t} c_{\omega_t}\right)}{r_t}\right) - \frac{2p_c}{{r_c}^2}\left(c_{\theta_c}{p_c}^2 + 2a_c e_c r_c\right)\times \\ & \left(c_{\Omega_c} s_{\theta_c} s_{\omega_c} - c_{\Omega_c} c_{\theta_c} c_{\omega_c} + s_{\Omega_c} c_{i_c} c_{\theta_c} s_{\omega_c} + s_{\Omega_c} c_{i_c} c_{\omega_c} s_{\theta_c}\right)\times \\ & \left(\frac{{p_c}^2 c_{\theta_c}\left(c_{\Omega_c} c_{\omega_c} - s_{\Omega_c} c_{i_c} s_{\omega_c}\right)}{r_c} - \frac{{p_t}^2 c_{\theta_t}\left(c_{\Omega_t} c_{\omega_t} - s_{\Omega_t} c_{i_t} s_{\omega_t}\right)}{r_t} \right. \\ & \left. - \frac{{p_c}^2 s_{\theta_c}\left(c_{\Omega_c} s_{\omega_c} + s_{\Omega_c} c_{i_c} c_{\omega_c}\right)}{r_c} + \frac{{p_t}^2 s_{\theta_t}\left(c_{\Omega_t} s_{\omega_t} + s_{\Omega_t} c_{i_t} c_{\omega_t}\right)}{r_t}\right) \\ & + \frac{2p_c}{{r_c}^3 r_t}\sin\left(\theta_c+\omega_c\right) s_{i_c}\left(c_{\theta_c}{p_c}^2 + 2a_c e_c r_c\right)\left({p_c}^2 r_t c_{\theta_c} s_{i_c} s_{\omega_c} \right. \\ & \left. + {p_c}^2 r_t c_{\omega_c} s_{i_c} s_{\theta_c} - {p_t}^2 r_c c_{\theta_t} s_{i_t} s_{\omega_t} - {p_t}^2 r_c c_{\omega_t} s_{i_t} s_{\theta_t}\right) \end{aligned} \tag{B.3}$$

$$\begin{aligned} H^2_{de,2} = & 2\left(\left(\frac{{p_c}^2 c_{\theta_c}\left(s_{\Omega_c} c_{\omega_c} + c_{\Omega_c} c_{i_c} s_{\omega_c}\right)}{r_c} - \frac{{p_t}^2 c_{\theta_t}\left(s_{\Omega_t} c_{\omega_t} + c_{\Omega_t} c_{i_t} s_{\omega_t}\right)}{r_t} \right. \right. \\ & \left. - \frac{{p_c}^2 s_{\theta_c}\left(s_{\Omega_c} s_{\omega_c} - c_{\Omega_c} c_{i_c} c_{\omega_c}\right)}{r_c} + \frac{{p_t}^2 s_{\theta_t}\left(s_{\Omega_t} s_{\omega_t} - c_{\Omega_t} c_{i_t} c_{\omega_t}\right)}{r_t}\right)^2 \\ & + \left(\frac{{p_c}^2 c_{\theta_c}\left(c_{\Omega_c} c_{\omega_c} - s_{\Omega_c} c_{i_c} s_{\omega_c}\right)}{r_c} - \frac{{p_t}^2 c_{\theta_t}\left(c_{\Omega_t} c_{\omega_t} - s_{\Omega_t} c_{i_t} s_{\omega_t}\right)}{r_t} \right. \\ & \left. - \frac{{p_c}^2 s_{\theta_c}\left(c_{\Omega_c} s_{\omega_c} + s_{\Omega_c} c_{i_c} c_{\omega_c}\right)}{r_c} + \frac{{p_t}^2 s_{\theta_t}\left(c_{\Omega_t} s_{\omega_t} + s_{\Omega_t} c_{i_t} c_{\omega_t}\right)}{r_t}\right)^2 \\ & + \frac{1}{{r_c}^2 {r_t}^2}\left({p_c}^2 r_t c_{\theta_c} s_{i_c} s_{\omega_c} + {p_c}^2 r_t c_{\omega_c} s_{i_c} s_{\theta_c} - {p_t}^2 r_c c_{\theta_t} s_{i_t} s_{\omega_t} \right. \\ & \left. \left. - {p_t}^2 r_c c_{\omega_t} s_{i_t} s_{\theta_t}\right)^2\right)^{3/2} \end{aligned} \tag{B.4}$$

$$
\begin{aligned}
H^2_{nu,3} = & -\frac{2{p_c}^2}{{r_c}^2 r_t}\sin\left(\theta_c+\omega_c\right)c_{i_c}\left({p_c}^2 r_t c_{\theta_c}s_{i_c}s_{\omega_c}+{p_c}^2 r_t c_{\omega_c}s_{i_c}s_{\theta_c}\right.\\
& \left.-{p_t}^2 r_c c_{\theta_t}s_{i_t}s_{\omega_t}-{p_t}^2 r_c c_{\omega_t}s_{i_t}s_{\theta_t}\right)-\frac{2{p_c}^2}{r_c}c_{\Omega_c}\sin\left(\theta_c+\omega_c\right)s_{i_c}\times\\
& \left(\frac{{p_c}^2 c_{\theta_c}\left(s_{\Omega_c}c_{\omega_c}+c_{\Omega_c}c_{i_c}s_{\omega_c}\right)}{r_c}-\frac{{p_t}^2 c_{\theta_t}\left(s_{\Omega_t}c_{\omega_t}+c_{\Omega_t}c_{i_t}s_{\omega_t}\right)}{r_t}\right.\\
& \left.-\frac{{p_c}^2 s_{\theta_c}\left(s_{\Omega_c}s_{\omega_c}-c_{\Omega_c}c_{i_c}c_{\omega_c}\right)}{r_c}+\frac{{p_t}^2 s_{\theta_t}\left(s_{\Omega_t}s_{\omega_t}-c_{\Omega_t}c_{i_t}c_{\omega_t}\right)}{r_t}\right)\\
& +\frac{2{p_c}^2}{r_c}\sin\left(\theta_c+\omega_c\right)s_{\Omega_c}s_{i_c}\left(\frac{{p_c}^2 c_{\theta_c}\left(c_{\Omega_c}c_{\omega_c}-s_{\Omega_c}c_{i_c}s_{\omega_c}\right)}{r_c}\right.\\
& -\frac{{p_t}^2 c_{\theta_t}\left(c_{\Omega_t}c_{\omega_t}-s_{\Omega_t}c_{i_t}s_{\omega_t}\right)}{r_t}-\frac{{p_c}^2 s_{\theta_c}\left(c_{\Omega_c}s_{\omega_c}+s_{\Omega_c}c_{i_c}c_{\omega_c}\right)}{r_c}\\
& \left.+\frac{{p_t}^2 s_{\theta_t}\left(c_{\Omega_t}s_{\omega_t}+s_{\Omega_t}c_{i_t}c_{\omega_t}\right)}{r_t}\right)
\end{aligned}
\tag{B.5}
$$

$$
\begin{aligned}
H^2_{de,3} = & 2\left(\left(\frac{{p_c}^2 c_{\theta_c}\left(s_{\Omega_c}c_{\omega_c}+c_{\Omega_c}c_{i_c}s_{\omega_c}\right)}{r_c}-\frac{{p_t}^2 c_{\theta_t}\left(s_{\Omega_t}c_{\omega_t}+c_{\Omega_t}c_{i_t}s_{\omega_t}\right)}{r_t}\right.\right.\\
& \left.-\frac{{p_c}^2 s_{\theta_c}\left(s_{\Omega_c}s_{\omega_c}-c_{\Omega_c}c_{i_c}c_{\omega_c}\right)}{r_c}+\frac{{p_t}^2 s_{\theta_t}\left(s_{\Omega_t}s_{\omega_t}-c_{\Omega_t}c_{i_t}c_{\omega_t}\right)}{r_t}\right)^2\\
& +\left(\frac{{p_c}^2 c_{\theta_c}\left(c_{\Omega_c}c_{\omega_c}-s_{\Omega_c}c_{i_c}s_{\omega_c}\right)}{r_c}-\frac{{p_t}^2 c_{\theta_t}\left(c_{\Omega_t}c_{\omega_t}-s_{\Omega_t}c_{i_t}s_{\omega_t}\right)}{r_t}\right.\\
& \left.-\frac{{p_c}^2 s_{\theta_c}\left(c_{\Omega_c}s_{\omega_c}+s_{\Omega_c}c_{i_c}c_{\omega_c}\right)}{r_c}+\frac{{p_t}^2 s_{\theta_t}\left(c_{\Omega_t}s_{\omega_t}+s_{\Omega_t}c_{i_t}c_{\omega_t}\right)}{r_t}\right)^2\\
& +\frac{1}{{r_c}^2{r_t}^2}\left({p_c}^2 r_t c_{\theta_c}s_{i_c}s_{\omega_c}+{p_c}^2 r_t c_{\omega_c}s_{i_c}s_{\theta_c}-{p_t}^2 r_c c_{\theta_t}s_{i_t}s_{\omega_t}\right.\\
& \left.\left.-{p_t}^2 r_c c_{\omega_t}s_{i_t}s_{\theta_t}\right)^2\right)^{3/2}
\end{aligned}
\tag{B.6}
$$

$$
\begin{aligned}
H^2_{nu,4} = & 2\left(\frac{{p_c}^2 c_{\theta_c}\left(c_{\Omega_c}s_{\omega_c}+s_{\Omega_c}c_{i_c}c_{\omega_c}\right)}{r_c}+\frac{{p_c}^2 s_{\theta_c}\left(c_{\Omega_c}c_{\omega_c}-s_{\Omega_c}c_{i_c}s_{\omega_c}\right)}{r_c}\right)\times\\
& \left(\frac{{p_c}^2 c_{\theta_c}\left(c_{\Omega_c}c_{\omega_c}-s_{\Omega_c}c_{i_c}s_{\omega_c}\right)}{r_c}-\frac{{p_t}^2 c_{\theta_t}\left(c_{\Omega_t}c_{\omega_t}-s_{\Omega_t}c_{i_t}s_{\omega_t}\right)}{r_t}\right.\\
& \left.-\frac{{p_c}^2 s_{\theta_c}\left(c_{\Omega_c}s_{\omega_c}+s_{\Omega_c}c_{i_c}c_{\omega_c}\right)}{r_c}+\frac{{p_t}^2 s_{\theta_t}\left(c_{\Omega_t}s_{\omega_t}+s_{\Omega_t}c_{i_t}c_{\omega_t}\right)}{r_t}\right)\\
& +2\left(\frac{{p_c}^2 c_{\theta_c}\left(s_{\Omega_c}s_{\omega_c}-c_{\Omega_c}c_{i_c}c_{\omega_c}\right)}{r_c}+\frac{{p_c}^2 s_{\theta_c}\left(s_{\Omega_c}c_{\omega_c}+c_{\Omega_c}c_{i_c}s_{\omega_c}\right)}{r_c}\right)\times\\
& \left(\frac{{p_c}^2 c_{\theta_c}\left(s_{\Omega_c}c_{\omega_c}+c_{\Omega_c}c_{i_c}s_{\omega_c}\right)}{r_c}-\frac{{p_t}^2 c_{\theta_t}\left(s_{\Omega_t}c_{\omega_t}+c_{\Omega_t}c_{i_t}s_{\omega_t}\right)}{r_t}\right.\\
& \left.-\frac{{p_c}^2 s_{\theta_c}\left(s_{\Omega_c}s_{\omega_c}-c_{\Omega_c}c_{i_c}c_{\omega_c}\right)}{r_c}+\frac{{p_t}^2 s_{\theta_t}\left(s_{\Omega_t}s_{\omega_t}-c_{\Omega_t}c_{i_t}c_{\omega_t}\right)}{r_t}\right)
\end{aligned}
\tag{B.7}
$$

$$
\begin{aligned}
& -2\left(\frac{{p_c}^2 c_{\theta_c}c_{\omega_c}s_{i_c}}{r_c}-\frac{{p_c}^2 s_{i_c}s_{\theta_c}s_{\omega_c}}{r_c}\right)\left(\frac{{p_c}^2 c_{\theta_c}s_{i_c}s_{\omega_c}}{r_c}+\frac{{p_c}^2 c_{\omega_c}s_{i_c}s_{\theta_c}}{r_c}\right.\\
& \left.-\frac{{p_t}^2 c_{\theta_t}s_{i_t}s_{\omega_t}}{r_t}-\frac{{p_t}^2 c_{\omega_t}s_{i_t}s_{\theta_t}}{r_t}\right)
\end{aligned}
\tag{B.8}
$$

$$
\begin{aligned}
H^2_{de,4} = & 2\left(\left(\frac{{p_c}^2 c_{\theta_c}s_{i_c}s_{\omega_c}}{r_c}+\frac{{p_c}^2 c_{\omega_c}s_{i_c}s_{\theta_c}}{r_c}-\frac{{p_t}^2 c_{\theta_t}s_{i_t}s_{\omega_t}}{r_t}-\frac{{p_t}^2 c_{\omega_t}s_{i_t}s_{\theta_t}}{r_t}\right)^2\right.\\
& +\left(\frac{{p_c}^2 c_{\theta_c}\left(s_{\Omega_c}c_{\omega_c}+c_{\Omega_c}c_{i_c}s_{\omega_c}\right)}{r_c}-\frac{{p_t}^2 c_{\theta_t}\left(s_{\Omega_t}c_{\omega_t}+c_{\Omega_t}c_{i_t}s_{\omega_t}\right)}{r_t}\right.\\
& \left.-\frac{{p_c}^2 s_{\theta_c}\left(s_{\Omega_c}s_{\omega_c}-c_{\Omega_c}c_{i_c}c_{\omega_c}\right)}{r_c}+\frac{{p_t}^2 s_{\theta_t}\left(s_{\Omega_t}s_{\omega_t}-c_{\Omega_t}c_{i_t}c_{\omega_t}\right)}{r_t}\right)^2\\
& +\left(\frac{{p_c}^2 c_{\theta_c}\left(c_{\Omega_c}c_{\omega_c}-s_{\Omega_c}c_{i_c}s_{\omega_c}\right)}{r_c}-\frac{{p_t}^2 c_{\theta_t}\left(c_{\Omega_t}c_{\omega_t}-s_{\Omega_t}c_{i_t}s_{\omega_t}\right)}{r_t}\right.\\
& \left.\left.\left.-\frac{{p_c}^2 s_{\theta_c}\left(c_{\Omega_c}s_{\omega_c}+s_{\Omega_c}c_{i_c}c_{\omega_c}\right)}{r_c}+\frac{{p_t}^2 s_{\theta_t}\left(c_{\Omega_t}s_{\omega_t}+s_{\Omega_t}c_{i_t}c_{\omega_t}\right)}{r_t}\right)^2\right)^{3/2}
\end{aligned}
\tag{B.9}
$$

$$
\begin{aligned}
H^2_{nu,5} = & 2\left(\frac{{p_c}^2 c_{\theta_c}\left(s_{\Omega_c}c_{\omega_c}+c_{\Omega_c}c_{i_c}s_{\omega_c}\right)}{r_c}-\frac{{p_c}^2 s_{\theta_c}\left(s_{\Omega_c}s_{\omega_c}-c_{\Omega_c}c_{i_c}c_{\omega_c}\right)}{r_c}\right)\times\\
& \left(\frac{{p_c}^2 c_{\theta_c}\left(c_{\Omega_c}c_{\omega_c}-s_{\Omega_c}c_{i_c}s_{\omega_c}\right)}{r_c}-\frac{{p_t}^2 c_{\theta_t}\left(c_{\Omega_t}c_{\omega_t}-s_{\Omega_t}c_{i_t}s_{\omega_t}\right)}{r_t}\right.\\
& \left.-\frac{{p_c}^2 s_{\theta_c}\left(c_{\Omega_c}s_{\omega_c}+s_{\Omega_c}c_{i_c}c_{\omega_c}\right)}{r_c}+\frac{{p_t}^2 s_{\theta_t}\left(c_{\Omega_t}s_{\omega_t}+s_{\Omega_t}c_{i_t}c_{\omega_t}\right)}{r_t}\right)\\
& -2\left(\frac{{p_c}^2 c_{\theta_c}\left(c_{\Omega_c}c_{\omega_c}-s_{\Omega_c}c_{i_c}s_{\omega_c}\right)}{r_c}-\frac{{p_c}^2 s_{\theta_c}\left(c_{\Omega_c}s_{\omega_c}+s_{\Omega_c}c_{i_c}c_{\omega_c}\right)}{r_c}\right)\times\\
& \left(\frac{{p_c}^2 c_{\theta_c}\left(s_{\Omega_c}c_{\omega_c}+c_{\Omega_c}c_{i_c}s_{\omega_c}\right)}{r_c}-\frac{{p_t}^2 c_{\theta_t}\left(s_{\Omega_t}c_{\omega_t}+c_{\Omega_t}c_{i_t}s_{\omega_t}\right)}{r_t}\right.\\
& \left.-\frac{{p_c}^2 s_{\theta_c}\left(s_{\Omega_c}s_{\omega_c}-c_{\Omega_c}c_{i_c}c_{\omega_c}\right)}{r_c}+\frac{{p_t}^2 s_{\theta_t}\left(s_{\Omega_t}s_{\omega_t}-c_{\Omega_t}c_{i_t}c_{\omega_t}\right)}{r_t}\right)
\end{aligned}
\tag{B.10}
$$

$$
\begin{aligned}
H^2_{de,5} = & 2\left(\left(\frac{{p_c}^2 c_{\theta_c}s_{i_c}s_{\omega_c}}{r_c}+\frac{{p_c}^2 c_{\omega_c}s_{i_c}s_{\theta_c}}{r_c}-\frac{{p_t}^2 c_{\theta_t}s_{i_t}s_{\omega_t}}{r_t}-\frac{{p_t}^2 c_{\omega_t}s_{i_t}s_{\theta_t}}{r_t}\right)^2\right.\\
& +\left(\frac{{p_c}^2 c_{\theta_c}\left(s_{\Omega_c}c_{\omega_c}+c_{\Omega_c}c_{i_c}s_{\omega_c}\right)}{r_c}-\frac{{p_t}^2 c_{\theta_t}\left(s_{\Omega_t}c_{\omega_t}+c_{\Omega_t}c_{i_t}s_{\omega_t}\right)}{r_t}\right.\\
& \left.-\frac{{p_c}^2 s_{\theta_c}\left(s_{\Omega_c}s_{\omega_c}-c_{\Omega_c}c_{i_c}c_{\omega_c}\right)}{r_c}+\frac{{p_t}^2 s_{\theta_t}\left(s_{\Omega_t}s_{\omega_t}-c_{\Omega_t}c_{i_t}c_{\omega_t}\right)}{r_t}\right)^2\\
& +\left(\frac{{p_c}^2 c_{\theta_c}\left(c_{\Omega_c}c_{\omega_c}-s_{\Omega_c}c_{i_c}s_{\omega_c}\right)}{r_c}-\frac{{p_t}^2 c_{\theta_t}\left(c_{\Omega_t}c_{\omega_t}-s_{\Omega_t}c_{i_t}s_{\omega_t}\right)}{r_t}\right.\\
& \left.\left.\left.-\frac{{p_c}^2 s_{\theta_c}\left(c_{\Omega_c}s_{\omega_c}+s_{\Omega_c}c_{i_c}c_{\omega_c}\right)}{r_c}+\frac{{p_t}^2 s_{\theta_t}\left(c_{\Omega_t}s_{\omega_t}+s_{\Omega_t}c_{i_t}c_{\omega_t}\right)}{r_t}\right)^2\right)^{3/2}
\end{aligned}
\tag{B.11}
$$

$$
\begin{aligned}
H^2_{nu,6} = 2\Bigg(& \frac{{p_c}^2 c_{\theta_c}\left(s_{\Omega_c} c_{\omega_c} + c_{\Omega_c} c_{i_c} s_{\omega_c}\right)}{r_c} - \frac{{p_t}^2 c_{\theta_t}\left(s_{\Omega_t} c_{\omega_t} + c_{\Omega_t} c_{i_t} s_{\omega_t}\right)}{r_t} \\
& - \frac{{p_c}^2 s_{\theta_c}\left(s_{\Omega_c} s_{\omega_c} - c_{\Omega_c} c_{i_c} c_{\omega_c}\right)}{r_c} + \frac{{p_t}^2 s_{\theta_t}\left(s_{\Omega_t} s_{\omega_t} - c_{\Omega_t} c_{i_t} c_{\omega_t}\right)}{r_t} \Bigg) \times \\
& \Bigg(\frac{{p_c}^2 c_{\theta_c}\left(s_{\Omega_c} s_{\omega_c} - c_{\Omega_c} c_{i_c} c_{\omega_c}\right)}{r_c} + \frac{{p_c}^2 s_{\theta_c}\left(s_{\Omega_c} c_{\omega_c} + c_{\Omega_c} c_{i_c} s_{\omega_c}\right)}{r_c} \\
& + \frac{e_c {p_c}^3 s_{\theta_c}{}^2\left(s_{\Omega_c} s_{\omega_c} - c_{\Omega_c} c_{i_c} c_{\omega_c}\right)}{{r_c}^2} - \frac{e_c {p_c}^3 c_{\theta_c} s_{\theta_c}\left(s_{\Omega_c} c_{\omega_c} + c_{\Omega_c} c_{i_c} s_{\omega_c}\right)}{{r_c}^2} \Bigg) \\
& + 2\Bigg(\frac{{p_c}^2 c_{\theta_c}\left(c_{\Omega_c} c_{\omega_c} - s_{\Omega_c} c_{i_c} s_{\omega_c}\right)}{r_c} - \frac{{p_t}^2 c_{\theta_t}\left(c_{\Omega_t} c_{\omega_t} - s_{\Omega_t} c_{i_t} s_{\omega_t}\right)}{r_t} \\
& - \frac{{p_c}^2 s_{\theta_c}\left(c_{\Omega_c} s_{\omega_c} + s_{\Omega_c} c_{i_c} c_{\omega_c}\right)}{r_c} + \frac{{p_t}^2 s_{\theta_t}\left(c_{\Omega_t} s_{\omega_t} + s_{\Omega_t} c_{i_t} c_{\omega_t}\right)}{r_t} \Bigg) \times \\
& \Bigg(\frac{{p_c}^2 c_{\theta_c}\left(c_{\Omega_c} s_{\omega_c} + s_{\Omega_c} c_{i_c} c_{\omega_c}\right)}{r_c} + \frac{{p_c}^2 s_{\theta_c}\left(c_{\Omega_c} c_{\omega_c} - s_{\Omega_c} c_{i_c} s_{\omega_c}\right)}{r_c} \\
& + \frac{e_c {p_c}^3 s_{\theta_c}{}^2\left(c_{\Omega_c} s_{\omega_c} + s_{\Omega_c} c_{i_c} c_{\omega_c}\right)}{{r_c}^2} - \frac{e_c {p_c}^3 c_{\theta_c} s_{\theta_c}\left(c_{\Omega_c} c_{\omega_c} - s_{\Omega_c} c_{i_c} s_{\omega_c}\right)}{{r_c}^2} \Bigg) \\
& - \frac{2{p_c}^2}{{r_c}^3 r_t} s_{i_c} \left(r_c \cos\left(\theta_c + \omega_c\right) + \frac{e_c p_c c_{\omega_c}}{2} - \frac{e_c p_c \cos\left(2\theta_c + \omega_c\right)}{2} \right) \times \\
& \left({p_c}^2 r_t c_{\theta_c} s_{i_c} s_{\omega_c} + {p_c}^2 r_t c_{\omega_c} s_{i_c} s_{\theta_c} - {p_t}^2 r_c c_{\theta_t} s_{i_t} s_{\omega_t} - {p_t}^2 r_c c_{\omega_t} s_{i_t} s_{\theta_t} \right)
\end{aligned}
\tag{B.12}
$$

$$
\begin{aligned}
H^2_{de,6} = 2\Bigg(& \Bigg(\frac{{p_c}^2 c_{\theta_c}\left(s_{\Omega_c} c_{\omega_c} + c_{\Omega_c} c_{i_c} s_{\omega_c}\right)}{r_c} - \frac{{p_t}^2 c_{\theta_t}\left(s_{\Omega_t} c_{\omega_t} + c_{\Omega_t} c_{i_t} s_{\omega_t}\right)}{r_t} \\
& - \frac{{p_c}^2 s_{\theta_c}\left(s_{\Omega_c} s_{\omega_c} - c_{\Omega_c} c_{i_c} c_{\omega_c}\right)}{r_c} + \frac{{p_t}^2 s_{\theta_t}\left(s_{\Omega_t} s_{\omega_t} - c_{\Omega_t} c_{i_t} c_{\omega_t}\right)}{r_t} \Bigg)^2 \\
& + \Bigg(\frac{{p_c}^2 c_{\theta_c}\left(c_{\Omega_c} c_{\omega_c} - s_{\Omega_c} c_{i_c} s_{\omega_c}\right)}{r_c} - \frac{{p_t}^2 c_{\theta_t}\left(c_{\Omega_t} c_{\omega_t} - s_{\Omega_t} c_{i_t} s_{\omega_t}\right)}{r_t} \\
& - \frac{{p_c}^2 s_{\theta_c}\left(c_{\Omega_c} s_{\omega_c} + s_{\Omega_c} c_{i_c} c_{\omega_c}\right)}{r_c} + \frac{{p_t}^2 s_{\theta_t}\left(c_{\Omega_t} s_{\omega_t} + s_{\Omega_t} c_{i_t} c_{\omega_t}\right)}{r_t} \Bigg)^2 \\
& + \frac{1}{{r_c}^2 {r_t}^2} \left({p_c}^2 r_t c_{\theta_c} s_{i_c} s_{\omega_c} + {p_c}^2 r_t c_{\omega_c} s_{i_c} s_{\theta_c} - {p_t}^2 r_c c_{\theta_t} s_{i_t} s_{\omega_t} \right. \\
& \left. - {p_t}^2 r_c c_{\omega_t} s_{i_t} s_{\theta_t} \right)^2 \Bigg)^{3/2}
\end{aligned}
\tag{B.13}
$$

References

[1] S. D'Amico, J.-S. Ardaens, R. Larsson, Spaceborne autonomous formation-flying experiment on the prisma mission, J. Guid. Control Dyn. 35 (3) (2012) 834–850, http://dx.doi.org/10.2514/1.55638.

[2] N.H. Roth, Navigation and Control Design for the Canx-4/-5 Satellite Formation Flying Mission (Ph.D. thesis), University of Toronto, 2010.

[3] J.K. Eyer, C. Damaren, R.E. Zee, E. Cannon, A formation flying control algorithm for the canx-4 & 5 low earth orbit nanosatellite mission, Space Technol. 27 (4) (2007) 147–158.

[4] G. Gaias, J.-S. Ardaens, Flight demonstration of autonomous noncooperative rendezvous in low earth orbit, J. Guid. Control Dyn. 41 (6) (2018) 1337–1354, http://dx.doi.org/10.2514/1.G003239.

[5] C.T. Fraser, S. Ulrich, Adaptive extended kalman filtering strategies for spacecraft formation relative navigation, Acta Astronaut. 178 (2021) 700–721, http://dx.doi.org/10.1016/j.actaastro.2020.10.016.

[6] D. Woffinden, D. Geller, Observability criteria for angles-only navigation, Aerosp. Electron. Syst. IEEE Trans. 45 (2009) 1194–1208, http://dx.doi.org/10.1109/TAES.2009.5259193.

[7] G. Gaias, S. D'Amico, J.-S. Ardaens, Angles-only navigation to a noncooperative satellite using relative orbital elements, J. Guid. Control Dyn. 37 (2) (2014) 439–451, http://dx.doi.org/10.2514/1.61494.

[8] S.C. Nardone, V.J. Aidala, Observability criteria for bearings-only target motion analysis, IEEE Trans. Aerosp. Electron. Syst. AES 17 (2) (1981) 162–166, http://dx.doi.org/10.1109/TAES.1981.309141.

[9] S.E. Hammel, V.J. Aidala, Observability requirements for three-dimensional tracking via angle measurements, IEEE Trans. Aerosp. Electron. Syst. AES 21 (2) (1985) 200–207, http://dx.doi.org/10.1109/TAES.1985.310617.

[10] J. Sullivan, S. D'Amico, Nonlinear Kalman filtering for improved angles-only navigation using relative orbital elements, J. Guid. Control Dyn. 40 (9) (2017) 2183–2200, http://dx.doi.org/10.2514/1.G002719.

[11] J. Sullivan, A.W. Koenig, J. Kruger, S. D'Amico, Generalized angles-only navigation architecture for autonomous distributed space systems, J. Guid. Control Dyn. 44 (6) (2021) 1087–1105, http://dx.doi.org/10.2514/1.G005439.

[12] H. Schaub, J.L. Junkins, Analytical Mechanics of Space Systems, AIAA American Institute of Aeronautics & Astronautics, 2018, pp. 593–673.

[13] K. Myers, B. Tapley, Adaptive sequential estimation with unknown noise statistics, IEEE Trans. Autom. Control 21 (4) (1976) 520–523, http://dx.doi.org/10.1109/TAC.1976.1101260.

[14] Y. Chihabi, S. Ulrich, Linear time-varying state transition matrix for spacecraft relative dynamics on highly elliptical orbits, Acta Astronaut. 198 (2022) 208–224, http://dx.doi.org/10.1016/j.actaastro.2022.05.056.

[15] Y. Chihabi, S. Ulrich, Hybrid guardian map-based adaptive control of spacecraft formation flying on highly elliptical orbits in the restricted three-body problem, Acta Astronaut. 180 (2021) 370–385, http://dx.doi.org/10.1016/j.actaastro.2020.12.048.

[16] P. Gurfil, K.V. Kholshevnikov, Manifolds and metrics in the relative spacecraft motion problem, J. Guid. Control Dyn. 29 (4) (2006) 1004–1010, http://dx.doi.org/10.2514/1.15531.

[17] G. Welch, G. Bishop, An Introduction to the Kalman Filter, Department of Computer Science, University of North Carolina, Chapel Hill.

[18] E. Wan, R. Van Der Merwe, The unscented Kalman filter for nonlinear estimation, in: Proceedings of the IEEE 2000 Adaptive Systems for Signal Processing, Communications, and Control Symposium (Cat. No. 00EX373), 2000, pp. 153–158, http://dx.doi.org/10.1109/ASSPCC.2000.882463.

[19] S.J. Julier, J.K. Uhlmann, New extension of the Kalman filter to nonlinear systems, in: Defense, Security, and Sensing, 1997.

[20] V.A. Bavdekar, A.P. Deshpande, S.C. Patwardhan, Identification of process and measurement noise covariance for state and parameter estimation using extended Kalman filter, J. Process Control 21 (4) (2011) 585–601, http://dx.doi.org/10.1016/j.jprocont.2011.01.001.

[21] H.E. Rauch, F. Tung, C.T. Striebel, Maximum likelihood estimates of linear dynamic systems, AIAA J. 3 (8) (1965) 1445–1450, http://dx.doi.org/10.2514/3.3166.

[22] Y. Chihabi, S. Ulrich, Spacecraft formation guidance law using a state transition matrix with gravitational, drag and third-body perturbations, in: 30th AIAA/AAS Space Flight Mechanics Meeting.

[23] Y. Chihabi, S. Ulrich, Software-in-the-loop validation of a novel two-point optimal guidance for perturbed spacecraft rendezvous and formations, J. Astronaut. Sci. 70 (43) (2023) http://dx.doi.org/10.1007/s40295-023-00405-8.

[24] G. Petit, B. Luzum, Iers Conventions, Tech. Rep., Frankfurt am Main: Verlag des Bundesamts für Kartographie und Geodäsie, 2010.

[25] R.C. Domingos, R.V. deMoraes, A.F.B.D.A. Prado, Third-body perturbation in the case of elliptic orbits for the disturbing bodies, Math. Probl. Eng. (2008) http://dx.doi.org/10.1155/2008/763654.

[26] A.F.B.A. Prado, Third-body perturbation in orbits around natural satellites, J. Guid. Control Dyn. 26 (1) (2003) 33–40, http://dx.doi.org/10.1155/2008/763654.

[27] O. Montenbruck, E. Gill, Satellite Orbits: Models, Methods, and Applications, Springer, 2001.

[28] T.V. Peters, J. Branco, D. Escorial, L.T. Castellani, A. Cropp, Mission analysis for proba-3 nominal operations, Acta Astronaut. 102 (2014) 296–310, http://dx.doi.org/10.1016/j.actaastro.2014.01.010.